GIANT

Incorporation of self-heating effect into a thermo-mechanical coupled constitutive modelling for elastomeric polyurethane

Jie Yang [a,b], **Zisheng Liao** [a,b], **Deepak George** [b], **Mokarram Hossain** [b,*], **Xiaohu Yao** [a,*]

a State Key Laboratory of Subtropical Building Science, South China University of Technology, Guangzhou 510640, China
b Zienkiewicz Institute for Modelling, Data and AI, Faculty of Science and Engineering, Swansea University, Swansea, SA1 8EN, United Kingdom

Elastomeric polyurethane (EPU) is characterised by distinctive mechanical properties, including high toughness, low glass transition temperature, and high impact resistance, that render it indispensable in diverse engineering applications from soft robotics to anti-collision devices. This study presents a thermo-mechanically coupled constitutive model for EPU, systematically incorporating hyperelasticity, viscoelasticity, thermal expansion, and self-heating effect in a thermodynamically consistent manner. Experimental data, obtained from previous studies, are then used for parameter identification and model validation, including iterative updates for temperature parameters considering the self-heating effect. Subsequently, the validated model is integrated into finite element codes, i.e., user subroutine to define a material's mechanical behaviour (UMAT) based on the commercial finite element software ABAQUS, for the computation of three-dimensional stress-strain states, facilitating the analysis of the structural response to various mechanical loads and boundary conditions. The results obtained from simulations are compared with analytical solutions to confirm the precision of Finite Element Method (FEM) implementation. The self-heating effect is further analysed under different strain rates and temperatures. To validate the engineering significance of the FEM implementation, a plate with a hole structure is also simulated. In conclusion, this research provides a robust tool for engineers and researchers working with soft materials, enhancing their understanding and predictive capabilities, notably addressing the self-heating effect in thermo-mechanical behaviours.

1 Introduction

Soft materials exhibit unique mechanical properties, including high toughness, low glass transition temperature, and high

impact resistance [1–5], making them indispensable in various engineering applications ranging from soft robotics to anti-collision devices. This work specifically focuses on elastomeric polyurethane (EPU), a soft polymer widely used in fields such as coatings, low-speed tyres, automobile carpets, and laminated windproof glass. The earliest experimental study of EPU may date back to the work of Petrović et al. [6] in 1991, and subsequent studies [3–5,7–19] have delved into more systematic experimental characterisation, including uniaxial tension, cyclic

* Corresponding authors.
   E-mail addresses: ctjyang@mail.scut.edu.cn (J. Yang), lzsheng2006@gmail.com (Z. Liao), 1916377@Swansea.ac.uk (D. George), mokarram.hossain@swansea.ac.uk (M. Hossain), yaoxh@scut.edu.cn (X. Yao).

loading, relaxation, and creep tests. Within these studies, typical inherent characteristics of EPU such as deformation nonlinearity, thermal sensitivity, rate sensitivity, and hysteresis have been experimentally detected.

As a theoretical tool for predicting material properties, constitutive models for soft materials have been a long-lasting focus due to the ever-increasing usage. These models can be roughly categorised into hyperelastic, viscoelastic, and thermo-viscoelastic constitutive models. Established hyperelastic models, such as the Neo-Hookean model, Mooney-Rivlin model [20], Ogden model [21], and eight-chain model [22], predominantly adopt phenomenological methods, assuming the presence of a strain energy function. As hyperelasticity alone is insufficient to capture the inherent time-dependent characteristics of soft materials, viscoelastic models are further developed. This field commonly employs three approaches: the decoupling method [23,24], the integration method [9,18,25–27], and the deformation gradient decomposition method [2–4,7,8,28–34]. However, while some models consider the thermo-mechanical behaviours of soft materials [4,35–43], the exploration of the constitutive models incorporating the self-heating effect remains inadequate. In a recent study, Felder et al [44] introduced a thermodynamical constitutive model incorporating heat generation to investigate semi-crystalline polymers, offering inspiration for the exploration of the thermal-mechanical behaviours of soft materials.

In accordance with the theoretical principles, the incorporation of constitutive models into finite element codes (e.g., UMAT), demands attention. Note that after the finite element method (FEM) implementation, user-developed constitutive model can be used for complex structures [45]. For implicit implementation, achieving rapid convergence hinges on the consistency of the stress tensor and tangent modulus tensor. This underscores the necessity for a rigorous three-dimensional generalisation of the constitutive models. The implementation of viscoelastic constitutive models presents additional challenges due to the consideration of evolution function solutions to the internal variables in three-dimensional domains [28,46]. Raghunath et al. [47] successfully used the concept of representative directions [48] to generalise a one-dimensional microstructure-based model into its three-dimensional case to describe the non-linear and viscoelastic mechanical behaviour of filled elastomers. The viscoelasticity is considered by using time-dependent parameters for the filler cluster. By using the perturbation method, [46,49,50], Collins et al. [51] numerically implemented a nonlinear viscoelastic framework into finite element codes to predict the viscous dissipation of a submerged elastomeric membrane. While some viscoelastic implementations have been explored, the complexity escalates when considering thermal behaviours such as heat generation and heat convection. The complexity arises from the additional consideration of the heat conduction equations, necessitating simultaneous solutions of the deformation field and the temperature field. Sharma et al. [37] reported a three-dimensional finite element framework based on the coupled nonlinear theory of thermo-electro-elasticity, investigating thermal effects on the electromechanical performance of non-homogeneously deforming dielectric elastomer actuators. The self-heating effect is another challenge that lacks enough focus. OvalleRodas et al. [52] developed a thermo-visco-hyperelastic constitutive model in accordance with the second law of thermodynamics for elastomeric materials. This model was subsequently implemented into finite element codes to describe the time-dependent and self-heating behaviour during low-cycle fatigue. The combined influence of temperature and strain rate on the mechanical behaviour is also investigated by Johnsen et al. [53] in simulating a low-density cross-linked polyurethane, incorporating thermo-elastic, thermo-viscoplastic, and entropic strain hardening parts. After the implementation, the volumetric strain, local strain rate, and self-heating can be observed in the tensile simulations. Felder et al. [44] implemented their thermo-mechanically coupled constitutive model, incorporating heat generation for semi-crystalline polymers, into the finite element framework so that their developed complex crystallisation phenomena can be validated in a structural example with sufficient accuracy.

However, there remains a gap in the existing literature concerning the systematic consideration of the temperature dependence and self-heating effect in soft materials especially in low-temperature cases. Therefore, this study endeavours to employ a thorough methodology to investigate the thermo-mechanical behaviour of EPU. Initially, the experimental performance of EPU at different temperatures is presented and a thermo-mechanically coupled constitutive model reproducing these material performances is introduced based on continuum mechanics and thermodynamics. This model considers not only the hyperelasticity and viscoelasticity inherent in EPU (same practice as [5]), but further, thermo-mechanical coupling response, along with the incorporation of the self-heating effect. After parameter identification and model validation, the constitutive model is implemented into a finite element framework, allowing for a comprehensive exploration of the self-heating effect in FEM simulations. Our objective is to furnish engineers and researchers working with soft materials with a valuable tool for understanding and predicting thermo-mechanical behaviour under diverse circumstances, with a particular emphasis on scenarios where self-heating is a key consideration.

The following is a breakdown of the structure of this study. In addition to the current section, Section 2 summarises the experimental setup and results from previous work. Subsequently, Section 3 specifies the derivation of the thermal-mechanically coupled constitutive model based on continuum mechanics and thermodynamics. Parameter identification and model validation are also included in this section. Further, Section 4 explains the implementation of the proposed constitutive model into the FEM framework, and then a plate with a hole structure is used to further validate and demonstrate the structural performance of the FEM implementation. Finally, a summary of the results and conclusions is presented in Section 6.

2 Experimental setup and results

Before the derivation of the constitutive modelling, the thermo-mechanical experimental setup and results for EPU from [5]
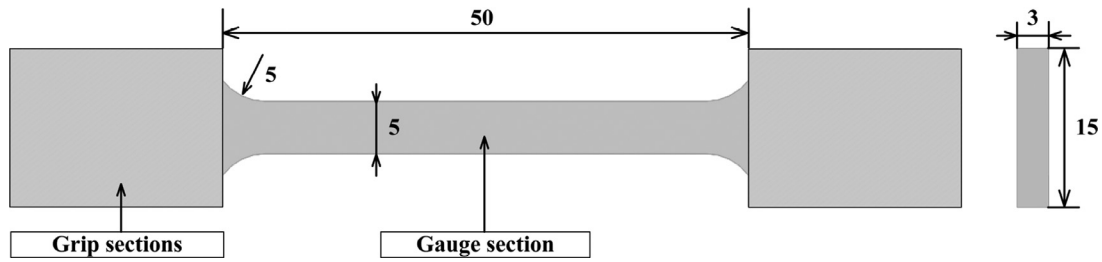
Fig. 1

The dimension of the specimen used in experiments [5].

Table 1

Experimental schedule [5].

Deformation mode	Strain rate	Relaxation time	Prescribed strain	Temperature			
				253K	273K	293K	333K
Loading-unloading uniaxial tensile test	0.001 /s	–	200%	–	–	●	–
	0.01 /s	–	200%	–	–	●	–
	0.1 /s	–	100%, 150%, 200%	●	●	●	●
Single-step stress relaxation	0.1 /s	6000 s	200%	●	●	●	●
Multi-step stress relaxation	0.1 /s	3600 s	25%, 50%,...,200%	–	–	●	–

are summarised briefly for completeness and clarity of this work.

2.1 Experimental setup

Dumbbell-shaped specimen is used in all of the experiments, with the geometry shown in Figure 1. All experiments are conducted according to the experimental schedule listed in Table 1 using an Instron 5567 universal test machine equipped with a bespoke temperature chamber. The experimental data is presented in the form of nominal stress and nominal strain. More experimental details can be seen in [5].

2.2 Experimental results

The main experimental data, that will be used in the constitutive modelling, is plotted in Figure 2. The purpose of these experiments is as follows:

- the single-step relaxation Figure 2(a): to explore the temperature influence on the hyperelastic entanglement network;
- the multi-step relaxation Figure 2(b): to extract the equilibrium path at referential temperature, i.e., 293K;
- the cyclic uniaxial tension: to investigate the rate-dependent Figure 2(c) and temperature-dependent Figure 2(d) viscoelastic mechanical behaviours.

3 Thermo-mechanical-coupled constitutive modelling at finite strains

One key step of the study is to incorporate a thermo-mechanically coupled constitutive model, accounting for the self-heating effect, into Finite Element Analysis for predicting the thermo-mechanical response of the EPU material and its applied structures. This model is introduced briefly here.

3.1 Kinematics

As the basis of continuum mechanics, kinematic relations are introduced first. In the context of soft materials, the classic multiplicative decomposition divides the deformation gradient $\mathbf{F}$ into isochoric part $\bar{\mathbf{F}}$ and volumetric part $\hat{\mathbf{F}}$ [28]. Furthermore, to facilitate a better understanding of the thermo-mechanically coupled framework, a rheology model of the isochoric deformation of our material is presented in Figure 3. As seen in this figure, the mechanical response is divided into two parallel parts, i.e., the hyperelastic branch and the viscoelastic branch. Note that these two branches share the same deformation gradient $\bar{\mathbf{F}}$ as they are in parallel. Regarding the deformation gradient $\bar{\mathbf{F}}$ of the viscoelastic branch, it is decomposed multiplicatively into two parts: the elastic part of the deformation gradient on the viscoelastic branch, $\mathbf{F}_e$ (represented by the spring in the viscoelastic branch in Figure 3), and the viscous part of the deformation gradient on the viscoelastic branch, $\mathbf{F}_v$ (represented by the dashpot in the viscoelastic branch in Figure 3). The decomposition relationship is $\bar{\mathbf{F}} = \mathbf{F}_e \mathbf{F}_v$ [4,51]. Using the relationship between the right Cauchy-Green strain tensor and the deformation gradient, we introduce $\mathbf{C}_e = \mathbf{F}_e^{\mathrm{T}} \mathbf{F}_e$ and $\mathbf{C}_v = \mathbf{F}_v^{\mathrm{T}} \mathbf{F}_v$, respectively. Note that the volumetric response, which will be discussed later, is determined based on the volume change of the body $J = \det\mathbf{F}$. Essential kinematics variables are declared in Table 2. For more details, refer to [5].

3.2 Stress derivation based on the Clausius-Duhem inequality

Here, the existence of a Helmholtz free-energy function, decomposed as

$$\Psi = \Psi^M + \Psi^\theta = \underbrace{\Psi_{\mathrm{iso}}^{\mathrm{EQ}}(\bar{\mathbf{C}}) + \Psi_{\mathrm{iso}}^{\mathrm{NEQ}}(\mathbf{C}^e, \theta) + \Psi_{\mathrm{vol}}(J)}_{\Psi^M} + \Psi^\theta(J, \theta), \quad (1)$$

is assumed. Note that in the above equation, "iso", "vol", "EQ", and "NEQ" denote the isochoric, volumetric, equilibrium, and non-equilibrium parts, $\mathbf{C}^e = \mathbf{F}_e^{\mathrm{T}} \mathbf{F}_e$ is the internal variable tensor and θ is the absolute temperature, respectively. To derive the constitutive model in a thermodynamic manner, the Clausius-
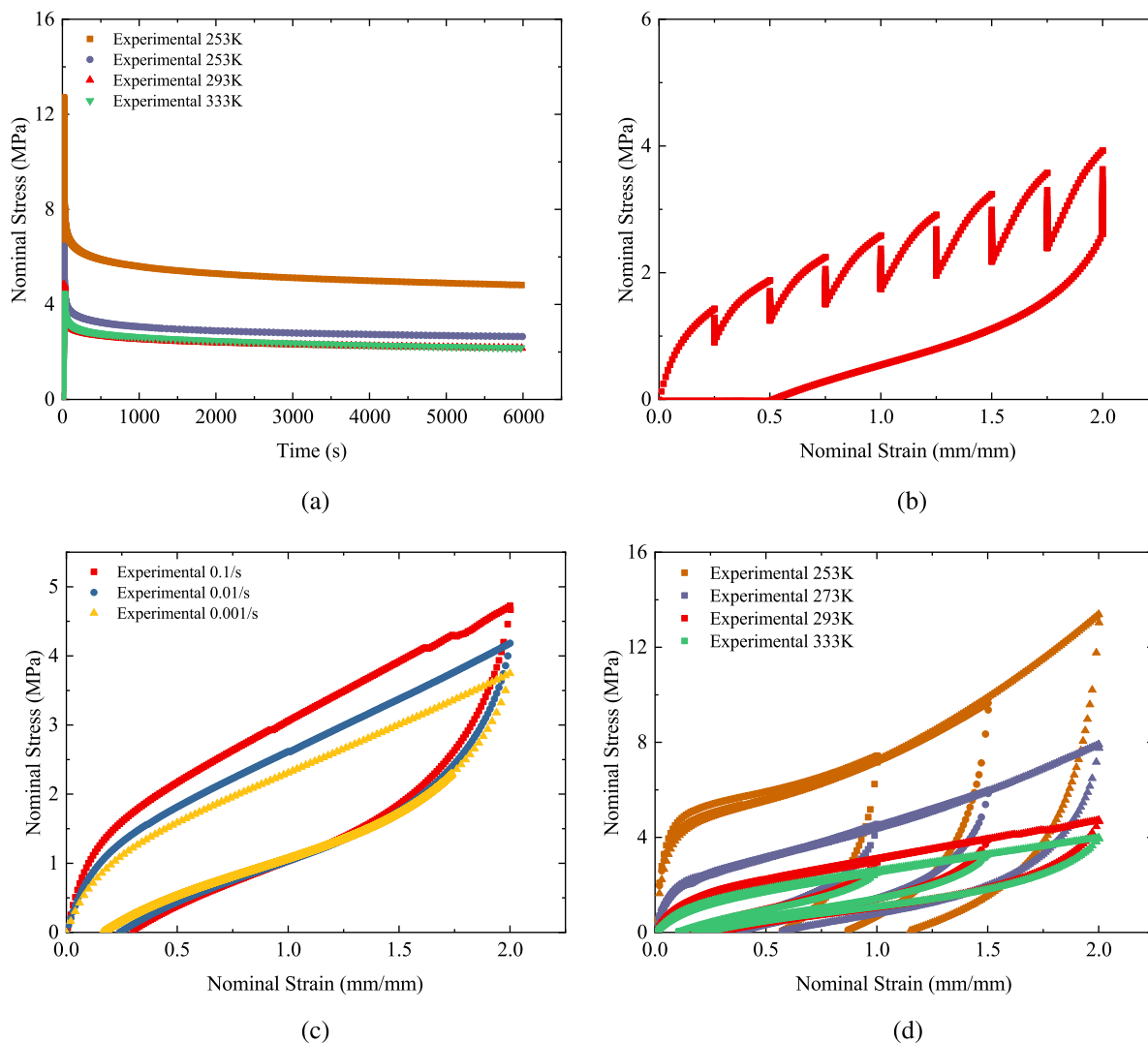
Fig. 2

Experimental data summary [5]. (a) Nominal stress with time relationships of the single-step relaxation tests at the strain of 200%. (b) Nominal stress with nominal strain relationship of the multi-step relaxation test under 293K. (c) Nominal stress with nominal strain relationships of loading-unloading tests at 0.1 /s, 0.01 /s, and 0.001 /s under 293K. (d) Nominal stress with nominal strain relationships of loading-unloading tests at 0.1 /s under 253K, 273K, 293K, and 333K.
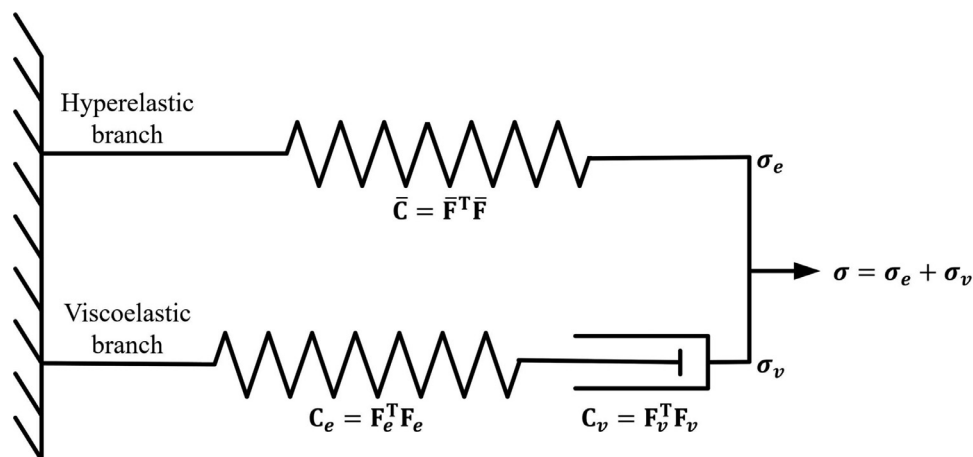

Fig. 3

The rheological model of isochoric deformation for elastomeric polyurethane. The model is divided into two parts, namely, hyperelastic branch and viscoelastic branch.

Table 2

A summary of the kinematics variables.

$\mathbf{F}$	$\frac{\partial \mathbf{x}}{\partial \mathbf{X}}$	The deformation gradient
$\mathbf{d}$	$\frac{1}{2}\left[\dot{\mathbf{F}}\mathbf{F}^{-1} + (\dot{\mathbf{F}}\mathbf{F}^{-1})^{\mathsf{T}}\right]$	The rate of deformation tensor
$\mathbf{C}$	$\mathbf{F}^{\mathsf{T}}\mathbf{F}$	The right Cauchy-Green strain tensor
$\dot{\mathbf{C}}$	$2\mathbf{F}^{\mathsf{T}}\mathbf{dF}$ [28]	The time rate of change of the right Cauchy-Green tensor
I_1	$\mathrm{tr}\mathbf{C}$	The first invariant of $\mathbf{C}$
I_2	$\frac{1}{2}\left[(\mathrm{tr}\mathbf{C})^2 - \mathrm{tr}(\mathbf{C}^2)\right]$	The second invariant of $\mathbf{C}$
I_3	$\det\mathbf{C}$	The third invariant of $\mathbf{C}$
J	$\det\mathbf{F}$	The volume change of the body
$\bar{\mathbf{F}}$	$(J^{-1/3})\mathbf{F}$	The volume-preserving deformation gradient
$\hat{\mathbf{F}}$	$(J^{1/3})\mathbf{I}$	The volume-changing deformation gradient
$\bar{\mathbf{C}}$	$(J^{-2/3})\mathbf{C}$	The modified right Cauchy-Green strain tensor
$\bar{I}_1$	$\mathrm{tr}\bar{\mathbf{C}}$	The first invariant of $\bar{\mathbf{C}}$
$\bar{I}_2$	$\frac{1}{2}\left[(\mathrm{tr}\bar{\mathbf{C}})^2 - \mathrm{tr}(\bar{\mathbf{C}}^2)\right]$	The second invariant of $\bar{\mathbf{C}}$
$\bar{I}_3$	$\det\bar{\mathbf{C}}$	The third invariant of $\bar{\mathbf{C}}$
$\mathbf{F}_e$	–	The elastic part of the deformation gradient on the viscoelastic branch
$\mathbf{F}_v$	–	The viscous part of the deformation gradient on the viscoelastic branch
$\mathbf{C}^e$	$\mathbf{F}_e^{\mathsf{T}}\mathbf{F}_e$	The right Cauchy-Green strain tensor of $\mathbf{F}_e$
$\mathbf{C}^v$	$\mathbf{F}_v^{\mathsf{T}}\mathbf{F}_v$	The right Cauchy-Green strain tensor of $\mathbf{F}_v$
I_1^e	$\mathrm{tr}\mathbf{C}^e$	The first invariant of $\mathbf{C}^e$
$\mathbf{d}_v$	$\frac{1}{2}\left[\dot{\mathbf{F}}_v\mathbf{F}_v^{-1} + (\dot{\mathbf{F}}_v\mathbf{F}_v^{-1})^{\mathsf{T}}\right]$	The viscous rate of deformation tensor

Table 3

A summary of the specific form of the constitutive framework at reference configuration.

Energy functions	Second Piola-Kirchhoff stresses
$\Psi = \Psi_{\mathrm{iso}}^{\mathrm{EQ}} + \Psi_{\mathrm{iso}}^{\mathrm{NEQ}} + \Psi_{\mathrm{vol}} + \Psi^{\theta}$ (Equation 1)	$\mathbf{S} = \mathbf{S}_{\mathrm{iso}} + \mathbf{S}_{\mathrm{vol}} + \mathbf{S}^{\theta}$ (Equation 5), where $\mathbf{S}_{\mathrm{iso}} = J^{-2/3}\mathbb{P} : (\bar{\mathbf{S}}^{\mathrm{EQ}} + \bar{\mathbf{S}}^{\mathrm{NEQ}})$
$\Psi_{\mathrm{iso}}^{\mathrm{EQ}}(\bar{\mathbf{C}}) = \left[\frac{\theta}{\theta_0} + g^{\mathrm{EQ}}\right]\left[\bar{I}_1 + b\bar{I}_1^4 + c\sqrt{\bar{I}_2}\right]$	$\bar{\mathbf{S}}^{\mathrm{EQ}} = \left[\frac{\theta}{\theta_0} + g^{\mathrm{EQ}}\right]\left[\left[2a + 8b(\bar{I}_1)^3\right]\mathbf{I} + c\left[\bar{I}_1\mathbf{I} - \bar{\mathbf{C}}\right](\bar{I}_2)^{-\frac{1}{2}}\right]$
$\Psi_{\mathrm{iso}}^{\mathrm{NEQ}}(\mathbf{C}^e, \theta) = \left[\frac{\theta}{\theta_0} + g^{\mathrm{NEQ}}\right]\left[\sum_{j=1}^{2} c_j\left([I_1^e]_j - 3\right)\right]$	$\bar{\mathbf{S}}^{\mathrm{NEQ}} = \left[\frac{\theta}{\theta_0} + g^{\mathrm{NEQ}}\right]\left[\sum_{j=1}^{2} 2c_j\mathbf{C}_j^{-v}\right]$
$\Psi_{\mathrm{vol}}(J) = \frac{K}{2}(J-1)^2$	$\mathbf{S}_{\mathrm{vol}} = Jp^{\mathrm{vol}}\mathbf{C}^{-1}$, where $p^{\mathrm{vol}} = K(J-1)$
$\Psi^{\theta}(J, \theta) = c\left[\theta - \theta_0 - \theta\ln(\frac{\theta}{\theta_0})\right] - 3\alpha(\theta - \theta_0)\frac{\partial \Psi_{\mathrm{vol}}}{\partial J}$	$\mathbf{S}^{\theta} = Jp^{\theta}\mathbf{C}^{-1}$, where $p^{\theta} = -3\alpha K(\theta - \theta_0)$
Evolution functions $\dot{\mathbf{C}}_j^v = \frac{1}{\tau_j}\left[\bar{\mathbf{C}} - \mathbf{C}_j^v\right]$	The nonlinear relaxation time $\tau_1 = \tau_{11} + \tau_{12}\exp(-k_{13}\|\dot{\mathbf{d}}\|)(\bar{I}_1 - 3)$ $\tau_2 = \tau_{21} + \tau_{22}\exp(-k_{23}\|\dot{\mathbf{d}}\|)$

Duhem inequality reads

$$\mathbf{S} : \frac{1}{2}\dot{\mathbf{C}} - \dot{\Psi} - \eta\dot{\theta} - \frac{1}{\theta}\mathbf{Q} \cdot \mathrm{Grad}\theta \geq 0, \tag{2}$$

which is the expression of the second law of thermodynamics in continuum mechanics. In Equation 2, $\mathbf{S}$ is the second Piola-Kirchhoff stress tensor, η is the entropy density, $\mathbf{Q}$ is the heat flux, and $\mathrm{Grad}\theta$ is the temperature gradient, respectively.

Note that the definition of $\mathbf{C}^e$ shown in Table 2 gives the following relationship as

$$\dot{\mathbf{C}}^e = \mathbf{F}_v^{-\mathsf{T}}\dot{\bar{\mathbf{C}}}\mathbf{F}_v^{-1} - 2\mathbf{C}^e\mathbf{d}_v. \tag{3}$$

Then, as $\dot{\mathbf{C}}$ and $\dot{\theta}$ are arbitrary, following the argumentation by Coleman and Gurtin [54]

$$\begin{cases} \mathbf{S} = 2\frac{\partial \Psi_{\mathrm{iso}}^{\mathrm{EQ}}}{\partial \mathbf{C}} : \frac{\partial \bar{\mathbf{C}}}{\partial \mathbf{C}} + 2\mathbf{F}_v^{-1}\frac{\partial \Psi_{\mathrm{iso}}^{\mathrm{NEQ}}}{\partial \mathbf{C}^e}\mathbf{F}_v^{-\mathsf{T}} : \frac{\partial \bar{\mathbf{C}}}{\partial \mathbf{C}} + J\frac{\partial \Psi_{\mathrm{vol}}}{\partial J}\mathbf{C}^{-1} + J\frac{\partial \Psi^{\theta}}{\partial J}\mathbf{C}^{-1} & \text{(4a)} \\ \eta = -\left(\frac{\partial \Psi^{\theta}}{\partial \theta} + \frac{\partial \Psi_{\mathrm{iso}}^{\mathrm{NEQ}}}{\partial \theta}\right) & \text{(4b)} \\ 2\mathbf{C}^e\frac{\partial \Psi_{\mathrm{iso}}^{\mathrm{NEQ}}}{\partial \mathbf{C}^e} : \mathbf{d}_v \geq 0 & \text{(4c)} \\ -\frac{1}{\theta}\mathbf{Q} \cdot \mathrm{Grad}\theta \geq 0 & \text{(4d)} \end{cases}$$

where Equation 4c and Equation 4d satisfied Equation 2 sufficiently. Analogous to the decomposition of

Ψ,

$$\mathbf{S} = \mathbf{S}_{\mathrm{iso}} + \mathbf{S}_{\mathrm{vol}} + \mathbf{S}^{\theta}, \tag{5}$$

where isochoric stress

$$\mathbf{S}_{\mathrm{iso}} = J^{-2/3}\mathbb{P} : (\bar{\mathbf{S}}^{\mathrm{EQ}} + \bar{\mathbf{S}}^{\mathrm{NEQ}}), \tag{6}$$

volumetric stress

$$\mathbf{S}_{\mathrm{vol}} = Jp^{\mathrm{vol}}\mathbf{C}^{-1}, \tag{7}$$

and thermal stress

$$\mathbf{S}^{\theta} = Jp^{\theta}\mathbf{C}^{-1}, \tag{8}$$

respectively. Note that

$$\mathbb{P} = \mathbb{I} - \frac{1}{3}\mathbf{C}^{-1} \otimes \mathbf{C} \tag{9}$$

is the projection tensor,

$$\bar{\mathbf{S}}^{\mathrm{EQ}} = 2\frac{\partial \Psi_{\mathrm{iso}}^{\mathrm{EQ}}}{\partial \bar{\mathbf{C}}} \quad \text{and} \quad \bar{\mathbf{S}}^{\mathrm{NEQ}} = 2\mathbf{F}_v^{-1}\frac{\partial \Psi_{\mathrm{iso}}^{\mathrm{NEQ}}}{\partial \mathbf{C}^e}\mathbf{F}_v^{\mathsf{T}} \tag{10}$$

are the equilibrium and non-equilibrium parts of the fictitious second Piola-Kirchhoff stress tensor, and

$$p^{\mathrm{vol}} = \frac{\partial \Psi_{\mathrm{vol}}}{\partial J} \quad \text{and} \quad p^{\theta} = \frac{\partial \Psi^{\theta}}{\partial J} \tag{11}$$

are the different parts of hydrostatic pressure, respectively. Therefore, through this decomposition, different versions of Ψ only influence $\bar{\mathbf{S}}^{\text{EQ}}$, $\bar{\mathbf{S}}^{\text{NEQ}}$, p^{vol}, and p^{θ}, which are the crucial tensors that need to be derived.

3.3 Heat generation

Viscoelasticity is inevitably accompanied by a loss of the potential energy causing heat generation due to dissipation. It is important to underscore that the dissipation energy density concerning the reference configuration, which contributes to the strain-, time-, and stress-dependent heat generation in our constitutive framework (refer to Equation 4), is specifically derived as

$$R = 2\mathbf{C}^{e}\frac{\partial \Psi_{\text{iso}}^{\text{NEQ}}}{\partial \mathbf{C}^{e}} : \mathbf{d}_{\nu} \quad = \frac{1}{2}\bar{\mathbf{C}}\bar{\mathbf{S}}^{\text{NEQ}} : [\mathbf{C}^{\nu}]^{-1}\dot{\mathbf{C}}_{\nu} \geq 0. \tag{12}$$

Note that the expression $[\mathbf{C}^{\nu}]^{-1}$ denotes the inverse of internal variable $\mathbf{C}^{\nu}$. It should be emphasised that a similar expression is seen in [44] through the operation of the local form of the energy balance.

3.4 Evolution function for the internal variables

Considering the relationship between the rate of volume change and the rate of deformation tensor, i.e. $\dot{J} = J\text{tr}\mathbf{d}$ [28] and the assumed almost incompressibility of $\mathbf{C}^{e}$, we have $\text{tr}\mathbf{d}_{\nu} \approx 0$. Then, to satisfy the non-negativity of Equation 4c, it is reasonable to assume that

$$\mathbf{d}_{\nu} = \frac{2}{\eta} \frac{\partial \Psi_{\text{iso}}^{\text{NEQ}}}{\partial I_{1}^{e}}\text{DEV}(\mathbf{C}^{e}) \tag{13}$$

where

$$\text{DEV}(\bullet) = (\bullet) - \frac{1}{3}\text{tr}(\bullet)\mathbf{I} \tag{14}$$

is introduced to obtain the deviatoric part of $(\bullet)$. By using the pull-back operation, the evolution function of $\mathbf{C}^{\nu}$ can then be expressed as

$$\dot{\mathbf{C}}^{\nu} = \frac{4}{\eta}\frac{\partial \Psi_{\text{iso}}^{\text{NEQ}}}{\partial I_{1}^{e}}\left[\bar{\mathbf{C}} - \frac{1}{3}\left[\bar{\mathbf{C}} : [\mathbf{C}^{\nu}]^{-1}\right]\mathbf{C}^{\nu}\right]. \tag{15}$$

Further, if the low-rate case is considered, the linear form of the above evolution function is reasonably given as

$$\dot{\mathbf{C}}^{\nu} = \frac{1}{\tau}\left[\bar{\mathbf{C}} - \mathbf{C}^{\nu}\right], \tag{16}$$

where τ is the relaxation time.

3.5 Specific form

For convenience, the specific form of the proposed constitutive framework at the reference configuration is summarised in Table 3.

Explanations to Table 3 are given as follows:

- The hyperelastic part $\Psi_{\text{iso}}^{\text{EQ}}$: a modified phenomenological model originally developed in [55] is used to describe the isochoric hyperelastic deformation. a, b, and c are hyperelastic parameters. The introduction of the second invariant is necessary to describe highly nonlinear hyperelastic behaviour and make the model more expedient [56–58]. The temperature influence on the hyperelastic stress is considered by using a double-exponential amplification factor as

$$\text{g}^{\text{EQ}} = -\frac{\theta}{\theta_{0}} + n_{1}^{\text{EQ}}\exp(n_{2}^{\text{EQ}}\theta) + n_{3}^{\text{EQ}}\exp(n_{4}^{\text{EQ}}\theta), \tag{17}$$

where $\theta_{0}, n_{1}^{\text{EQ}}, n_{2}^{\text{EQ}}, n_{3}^{\text{EQ}}$, and n_{4}^{EQ} are reference temperature (293K in this study) and the temperature parameters, respectively.

- The viscoelastic part $\Psi_{\text{iso}}^{\text{NEQ}}$: this is a modified version of the Neo-Hookean model to describe the viscoelastic behaviour. c_{j} are the viscoelastic parameters. The temperature influence on the viscoelastic stress is assumed to be similar to [4] as

$$\text{g}^{\text{NEQ}} = -\frac{\theta}{\theta_{0}} + \frac{1}{2}[\tanh(\theta - T_{\text{s}}) + 1]\left(\frac{\theta}{\theta}\right)^{n_{1}^{\text{NEQ}}}$$
$$+ \frac{n_{3}^{\text{NEQ}}}{2}[-\tanh(\theta - T_{\text{s}}) + 1]\left[\left(\frac{\theta}{\theta}\right)^{n_{2}^{\text{NEQ}}} - 1\right]\exp\left(n_{4}^{\text{NEQ}}\|\mathbf{C}\|\right), \tag{18}$$

where n_{1}^{NEQ}, n_{2}^{NEQ}, n_{3}^{NEQ}, and n_{4}^{NEQ} are the temperature parameters and T_{s}=281.95K. Here, $\|\bullet\|$ denotes the norm of the tensor $\bullet$.

- The volumetric part Ψ_{vol}: a so-called penalty function is used to describe the volumetric deformation for mitigating the numerical difficulties and instabilities associated with enforcing material incompressibility in computational and finite element simulations [58]. K is the bulk modulus chosen as 2000MPa directly to promise almost incompressible behaviours. More available versions can be seen in [59–67].

- The temperature part Ψ^{θ}: two terms contributed from the increased internal energy $\left(c[\theta - \theta_{0} - \theta\ln(\frac{\theta}{\theta_{0}})]\right)$ and thermal expansion $\left(-3\alpha(\theta - \theta_{0})\frac{\partial \Psi_{\text{vol}}}{\partial J}\right)$ are introduced to complete the general structure of the thermodynamic potential [4,28,37,47]. c and α are the specific heat capacity and the thermal expansion coefficient, respectively.

3.6 One-dimensional reduction

This section aims to identify the constitutive parameters by the one-dimensional degenerated form of the proposed constitutive model.

3.6.1 Uniaxial tensile stress

The deformation gradient and the right Cauchy-Green deformation tensor, in the uniaxial case, are specifically given as

$$\mathbf{F} = \begin{bmatrix} \lambda & 0 & 0 \\ 0 & \lambda^{-1/2} & 0 \\ 0 & 0 & \lambda^{-1/2} \end{bmatrix} \quad \text{and} \quad \mathbf{C} = \begin{bmatrix} \lambda^{2} & 0 & 0 \\ 0 & \lambda^{-1} & 0 \\ 0 & 0 & \lambda^{-1} \end{bmatrix}, \tag{19}$$

respectively, where λ is the axial elongation during uniaxial tension process. While the thermal stress ($\mathbf{S}^{\theta}$) is not yet considered in the previous experiments, the nominal uniaxial tension stress, i.e., $P_{11} = F_{11}(S_{11} - pC_{11}^{-1})$ is decomposed into hyperelastic part P_{11}^{EQ} and viscoelastic part P_{11}^{NEQ}. The following consideration should be mentioned in the uniaxial reduction situation: the almost incompressibility is promised by using a scalar Lagrange multiplier p, which is determined by setting the lateral stress as zero, and this operation describes the volume behaviour of soft material indirectly [5]. Following the proposed constitutive model, the specific expressions of nominal stresses are finally given as

$$P_{11}^{\text{EQ}} = \left[\frac{\theta}{\theta_{0}} + \text{g}^{\text{EQ}}\right]\left[2a + 8b\left[\frac{2}{\lambda} + \lambda^{2}\right]^{3} + c\left[1 + 2\lambda^{3}\right]^{-\frac{1}{2}}\right]\left[\lambda - \frac{1}{\lambda^{2}}\right] \tag{20}$$

$$\text{and} \quad P_{11}^{\text{NEQ}} = \left[\frac{\theta}{\theta_{0}} + \text{g}^{\text{NEQ}}\right]\left[\sum_{j=1}^{2} 2c_{j}\left(\frac{\lambda}{(\lambda_{1,j}^{\nu})^{2}} - \frac{1}{(\lambda_{2,j}^{\nu})^{2}\lambda^{2}}\right)\right], \tag{21}$$
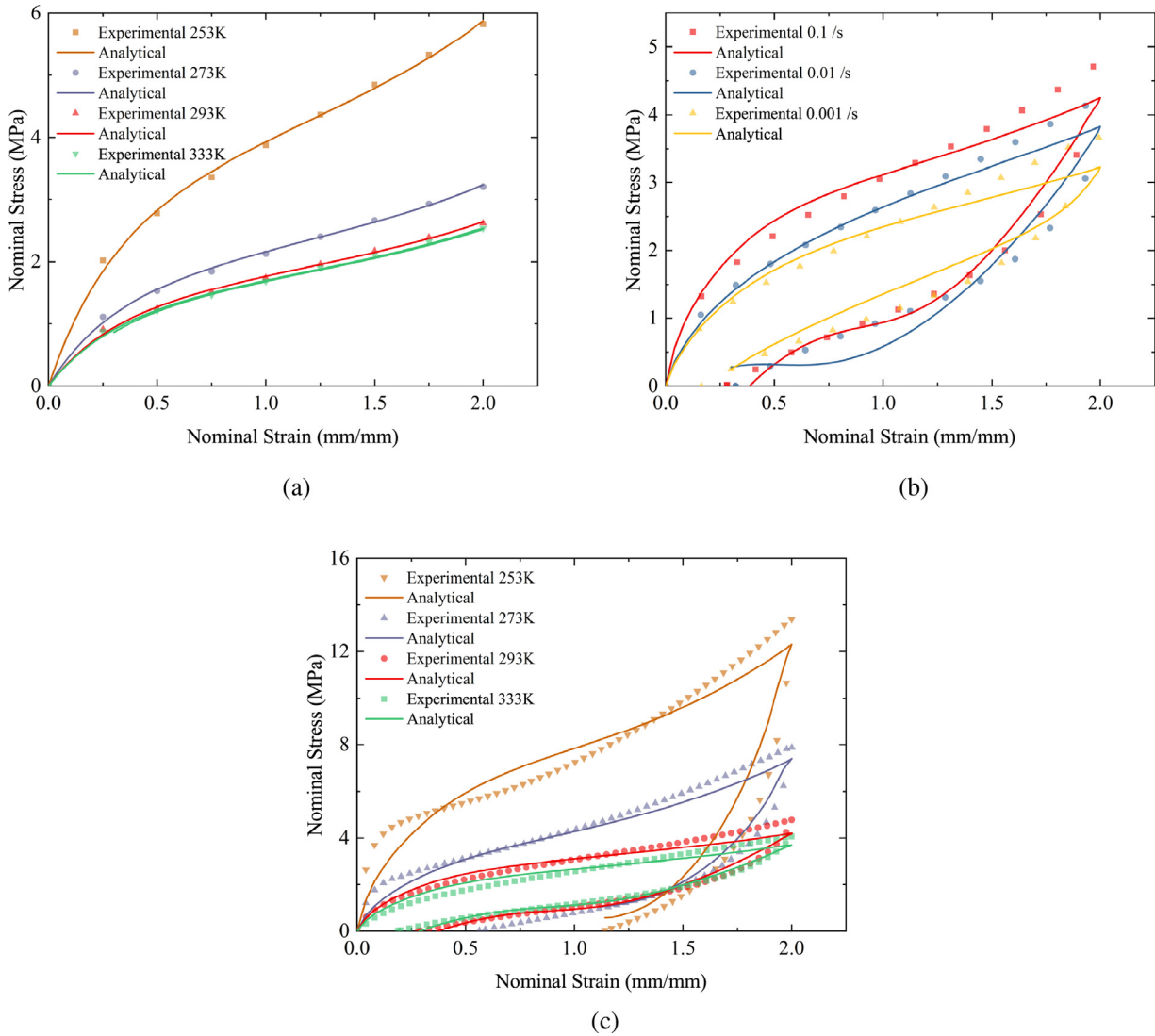
(a)

(b)

(c)

Fig. 4

Parameter identification for (a) hyperelastic part, (b) viscoelastic part, and (c) temperature part, respectively.

respectively, where $\lambda_{1,j}^v$, $\lambda_{2,j}^v$, and $\lambda_{3,j}^v$ are the eigenvalues of $[\mathbf{C}_j^v]^{1/2}$, respectively. Note that under the strict incompressible situation of internal variables, the above expressions can be simplified to the same form as the expressions shown in [5,51]. More discussion about the one-dimensional reduction of $\mathbf{C}^v$ is included in **Appendix: A**.

3.6.2 Parameter identification and model validation

Material parameter identification is then performed. Based on the codes written in `MATLAB` using the least squares method, the optimum series of parameters is found to fit the experimental data. The fitting results are seen in Figure 4, as well as the corresponding parameters listed in Table 4. Explanations about how experimental data are used for parameter identification are explained as follows.

① In the equilibrium part, the multi-step relaxation experimental data (see Figure 2(b)) is utilised to determine the hyperelastic parameters, as shown in Figure 4(a).

This experimental process involves stress decay as the system approaches the equilibrium state, allowing the extraction of the hyperelastic stress at every sub-relaxation point. Taking the data under 293K as the reference, the hyperelastic stresses under different temperatures are amplified according to the data from the single-step relaxation tests (see Figure 2(a)).

② In the non-equilibrium part, the data under different strain rates (see Figure 2(c)), i.e., 0.1/s, 0.01/s, and 0.001/s, are used to identify the viscoelastic parameters while keeping the hyperelastic stress constant, see Figure 4(b). Inside the algorithm, the Newton method is used to solve the evolution functions of the internal variables in the one-dimensional case.

③ In the temperature part, while keeping the hyperelastic and viscoelastic parameters frozen, the temperature parameters can be further identified by using the data under different temperatures (see Figure 2(d)), as illustrated in Figure 4(c).

Full-length article

Table 4

Constitutive model parameters.

Hyperelastic parameter	a [MPa]	b [MPa]	c [MPa]				
	2.85e-1	1.50e-5	1.74e0				
Viscoelastic parameter	c_1 [MPa]	τ_{11} [s]	τ_{12} [s]	k_{13} [s]	c_2 [MPa]	τ_{21} [s]	τ_{22} [s]	k_{23} [s]
	4.00e0	2.26e-14	9.88e0	5.55e+1	7.42e-1	1.30e1	2.54e3	3.01e3
Temperature parameter	n_1^{EQ} [-]	n_2^{EQ} [-]	n_3^{EQ} [-]	n_4^{EQ} [-]	n_1^{NEQ} [-]	n_2^{NEQ} [-]	n_3^{NEQ} [-]	n_4^{NEQ} [-]
	1.15e8	-7.22e-2	7.33e-1	7.96e-4	2.62e0	8.20e-4	1.44e+4	1.92e-1
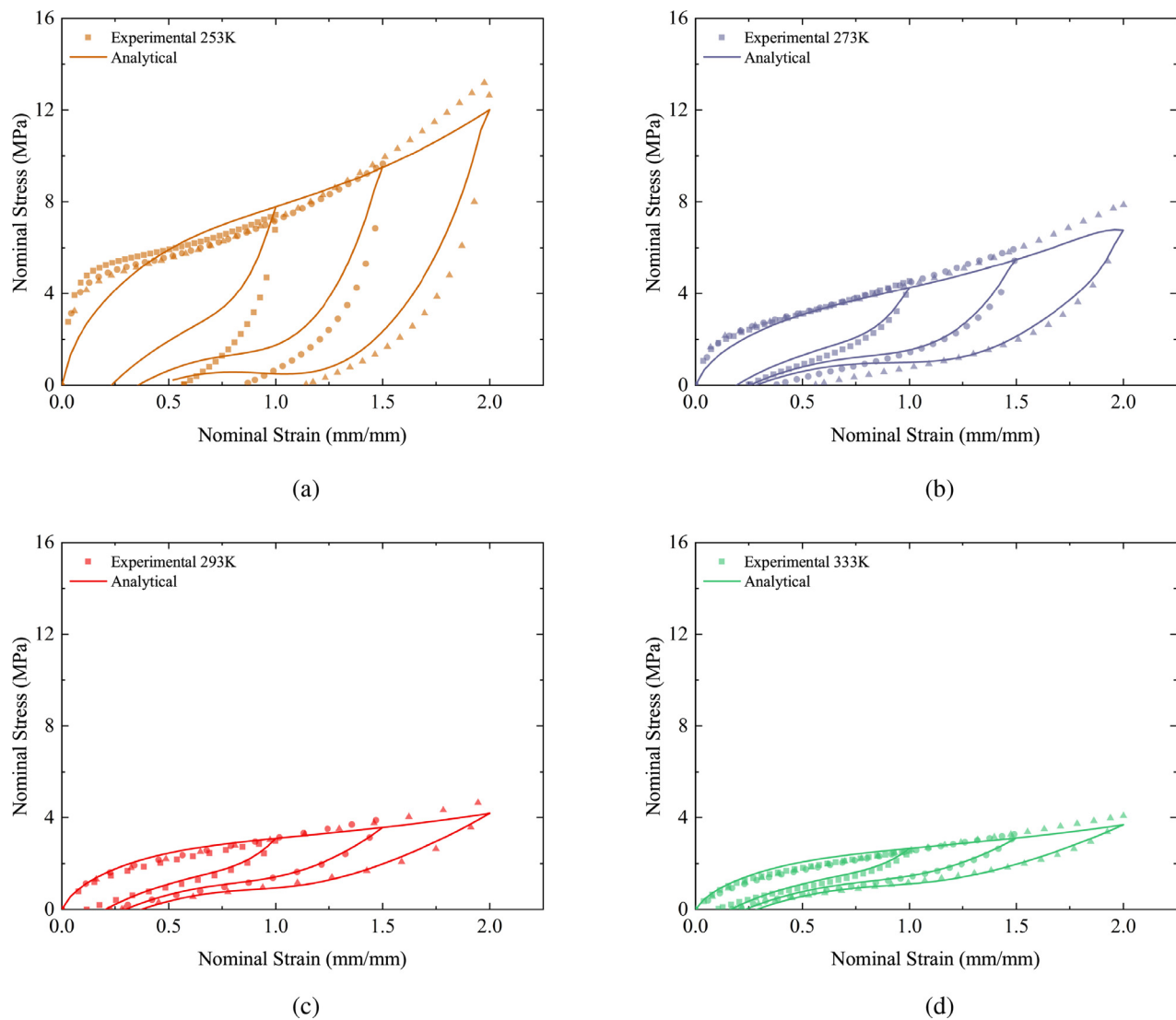
Fig. 5

Model validation under (a) 253K, (b) 273K, (c) 293K, and (d) 333K, respectively.

Here, we should note that the temperature parameters can not be identified simply without the consideration of temperature rise, i.e., the self-heating effect. While the actual temperature rise is currently unavailable, a local loop is needed for updating these parameters.

Model validation is performed by comparing the analytical results with the experimental data (has not been used in parameter identification), see Figure 5. As seen in these figures,

the experimental results are well captured by the proposed constitutive model as a whole.

4 Finite element implementation

In this section, a FEM framework is developed taking the aforementioned constitutive model, employing the user-material subroutine `UMAT` within the `ABAQUS/Standard` solver. It is important to note that for this coupling problem, the analysis

should be done within the subroutines of `UMAT` in combination with `UMATht` for `ABAQUS` versions released after 2020, otherwise, the subroutine `HETVAL` is necessitated [68].

4.1 Weak form of thermo-mechanical coupled constitutive equation

The nonlinear thermo-mechanical coupling problem is solved using an incremental-iterative strategy based on Newton-Raphson approach as [37]

$$\mathbb{K}_{\mathbf{uu}}\Delta\mathbf{u} + \mathbb{K}_{\mathbf{u}\theta}\Delta\theta = R_{\mathbf{u}}, \tag{22}$$

$$\mathbb{K}_{\theta\mathbf{u}}\Delta\mathbf{u} + \mathbb{K}_{\theta\theta}\Delta\theta = R_{\theta}, \tag{23}$$

where $\mathbb{K}_{\mathbf{uu}}$, $\mathbb{K}_{\mathbf{u}\theta}$, $\mathbb{K}_{\theta\mathbf{u}}$, $\mathbb{K}_{\theta\theta}$ are the components of Jacobian matrix, $\Delta\mathbf{u}$ is the displacement increment, $\Delta\theta$ is the temperature increment, and $R_{\mathbf{u}}$ and R_{θ} are the corresponding increments resulting from the displacement and temperature, respectively. Note that $\mathbb{K}_{\mathbf{u}\theta}$ and $\mathbb{K}_{\theta\mathbf{u}}$, despite being relatively small in most cases, are intentionally not omitted. Otherwise, the inaccuracy of the Jacobian matrix could lead to convergence issues.

4.1.1 Mechanical material laws

The solution of the governing equations using FEM requires the weak forms [37]. By considering the virtual displacement $\delta\mathbf{u}$, the weak form of energy balance integrating over the entire volume in the reference state is expressed as [28]

$$\int_{\Omega_0}\mathbf{S}:\frac{1}{2}\delta\mathbf{C}dV - \int_{\partial\Omega_0}\bar{\mathsf{T}}\cdot\delta\mathbf{u}dS - \int_{\Omega}\mathbf{B}\cdot\delta\mathbf{u}dV = 0, \tag{24}$$

where $\delta\mathbf{C} = \frac{1}{2}\big[(\mathbf{F}^{\mathrm{T}}\mathrm{Grad}\delta\mathbf{u})^{\mathrm{T}} + \mathbf{F}^{\mathrm{T}}\mathrm{Grad}\delta\mathbf{u}\big]$, $\bar{\mathsf{T}}$ denotes the prescribed first Piola-Kirchhoff traction, $\mathbf{B}$ is the reference body force, $\partial\Omega_0$ is the surface of the continuum Ω_0 at the referential configuration, respectively. For the thermo-mechanical coupling problem, the differential form of the second Piola-Kirchhoff stress tensor is

$$\mathrm{d}\mathbf{S}(\mathbf{C},\theta) = \mathbb{C}:\frac{1}{2}\mathrm{d}\mathbf{C} + \mathbf{T}\mathrm{d}\theta, \tag{25}$$

where

$$\mathbb{C} = 4\frac{\partial\Psi^2}{\partial\mathbf{C}\partial\mathbf{C}} \tag{26}$$

is the referential fourth-order elasticity tensor and

$$\mathbf{T} = 2\frac{\partial\Psi^2}{\partial\mathbf{C}\partial\theta} \tag{27}$$

is the referential second-order stress-temperature tensor, respectively. These two quantities measure the changes in stress which result from a change in strain and temperature, respectively. According to the relationship between Cauchy stress and second Piola-Kirchhoff stress, i.e., $\boldsymbol{\sigma} = J\mathbf{F}^{-1}\mathbf{S}\mathbf{F}^{-\mathrm{T}}$, as well as Equation 25, the rate-form constitutive law for Cauchy stress is derived as

$$\dot{\boldsymbol{\sigma}} = \left(2\boldsymbol{\sigma}\otimes\mathbf{I} + \frac{1}{J}\big[(\mathbf{F}\otimes\mathbf{F}^{\mathrm{T}}):\mathbb{C}:(\mathbf{F}^{\mathrm{T}}\otimes\mathbf{F})\big]\right):\mathbf{d} + \frac{1}{J}\mathbf{F}\mathbf{T}\mathbf{F}^{\mathrm{T}}\dot{\theta}. \tag{28}$$

As per the requirements for `UMAT`, the above equation gives the spatial Jaumann tangent moduli as

$$\overset{\triangledown}{\mathbb{C}} = 2\boldsymbol{\sigma}\otimes\mathbf{I} + \frac{1}{J}\big[(\mathbf{F}\otimes\mathbf{F}^{\mathrm{T}}):\mathbb{C}:(\mathbf{F}^{\mathrm{T}}\otimes\mathbf{F})\big] \tag{29}$$

and the spatial stress-temperature tensor as

$$\mathbf{t} = \frac{1}{J}\mathbf{F}\mathbf{T}\mathbf{F}^{\mathrm{T}}. \tag{30}$$

After the aforementioned derivation, the crucial aspects for the FEM implementation regarding the mechanical material laws are identified in the derivations of referential elasticity tensor $\mathbb{C}$ and referential stress-temperature tensor $\mathbf{T}$ of a specific form for the constitutive model (see Table 3).

Referential elasticity tensor

Following the characterisations of additive decomposition for the energy function and the stress tensor, the referential elasticity tensor is decomposed as

$$\mathbb{C} = \mathbb{C}_{\mathrm{iso}} + \mathbb{C}_{\mathrm{vol}} + \mathbb{C}^{\theta}. \tag{31}$$

According to the specific form shown in Table 3, the components of the referential elasticity tensor $\mathbb{C}$ are derived as follows.

• The isochoric part.

$$\begin{aligned}\mathbb{C}_{\mathrm{iso}} &= 2\frac{\partial\mathbf{S}_{\mathrm{iso}}}{\partial\mathbf{C}} = 2\frac{\partial(J^{-2/3}\mathbb{P}:\bar{\mathbf{S}})}{\partial\mathbf{C}}\\ &= \mathbb{P}:\bar{\mathbb{C}}:\mathbb{P}^{\mathrm{T}} + \frac{2}{3}\mathrm{Tr}\big(J^{-2/3}\bar{\mathbf{S}}\big)\tilde{\mathbb{P}} - \frac{2}{3}\big(\mathbf{C}^{-1}\otimes\mathbf{S}_{\mathrm{iso}} + \mathbf{S}_{\mathrm{iso}}\otimes\mathbf{C}^{-1}\big).\end{aligned} \tag{32}$$

Note that

$$\mathrm{Tr}(\bullet) = (\bullet):\mathbf{C}, \quad \tilde{\mathbb{P}} = \mathbf{C}^{-1}\odot\mathbf{C}^{-1} - \frac{1}{3}\mathbf{C}^{-1}\otimes\mathbf{C}^{-1},$$
$$\text{and} \quad \mathbf{C}^{-1}\odot\mathbf{C}^{-1} = -\frac{\partial\mathbf{C}^{-1}}{\partial\mathbf{C}}, \tag{33}$$

respectively. Furthermore, the fourth-order fictitious elasticity tensor

$$\bar{\mathbb{C}} = \bar{\mathbb{C}}^{\mathrm{EQ}} + \bar{\mathbb{C}}^{\mathrm{NEQ}}, \tag{34}$$

where

$$\begin{aligned}\bar{\mathbb{C}}^{\mathrm{EQ}} &= 2J^{-4/3}\frac{\partial\bar{\mathbf{S}}^{\mathrm{EQ}}}{\partial\bar{\mathbf{C}}}\\ &= 2J^{-4/3}\left[\frac{\theta}{\theta_0} + \mathrm{g}^{\mathrm{EQ}}\right]\Big(24b[\bar{I}_1]^2\mathbf{I}\otimes\mathbf{I} + c[\bar{I}_2]^{-\frac{1}{2}}[\mathbf{I}\otimes\mathbf{I} - \mathbb{I}]\\ &\quad -\frac{c}{2}[\bar{I}_2]^{-\frac{3}{2}}\big[\bar{I}_1\mathbf{I} - \bar{\mathbf{C}}\big]\otimes(\bar{I}_1\mathbf{I} - \bar{\mathbf{C}})\Big)\end{aligned} \tag{35}$$

and

$$\bar{\mathbb{C}}^{\mathrm{NEQ}} = 2J^{-4/3}\frac{\partial\bar{\mathbf{S}}^{\mathrm{NEQ}}}{\partial\bar{\mathbf{C}}} = 2J^{-4/3}\left[\frac{\theta}{\theta_0} + \mathrm{g}^{\mathrm{NEQ}}\right]\left[\sum_{j=1}^{2}2c_j\frac{\partial\mathbf{C}_j^{-v}}{\partial\bar{\mathbf{C}}}\right]. \tag{36}$$

• The volumetric part.

$$\mathbb{C}_{\mathrm{vol}} = 2\frac{\partial\mathbf{S}_{\mathrm{vol}}}{\partial\mathbf{C}} = (Jp^{\mathrm{vol}} + J^2\frac{\mathrm{d}p^{\mathrm{vol}}}{\mathrm{d}J})\mathbf{C}^{-1}\otimes\mathbf{C}^{-1} - 2Jp^{\mathrm{vol}}\mathbf{C}^{-1}\odot\mathbf{C}^{-1}. \tag{37}$$

• The thermal part.

$$\mathbb{C}^{\theta} = 2\frac{\partial\mathbf{S}^{\theta}}{\partial\mathbf{C}} = (Jp^{\theta} + J^2\frac{\mathrm{d}p^{\theta}}{\mathrm{d}J})\mathbf{C}^{-1}\otimes\mathbf{C}^{-1} - 2Jp^{\theta}\mathbf{C}^{-1}\odot\mathbf{C}^{-1}. \tag{38}$$

Referential stress-temperature tensor

Similarly, the referential stress-temperature tensor is decomposed as

$$\mathbf{T} = \mathbf{T}_{\mathrm{iso}} + \mathbf{T}_{\mathrm{vol}} + \mathbf{T}^{\theta}. \tag{39}$$

According to the specific form shown in Table 3, the components of the referential stress-temperature tensor $\mathbf{T}$ are derived as follows.

- The isochoric part.

$$\mathbf{T}_{\text{iso}} = \frac{\partial (J^{-2/3}\mathbb{P}:\bar{\mathbf{S}})}{\partial \theta} = J^{-2/3}\mathbb{P} : \bar{\mathbf{T}}, \quad \text{where} \quad \bar{\mathbf{T}} = \bar{\mathbf{T}}^{\text{EQ}} + \bar{\mathbf{T}}^{\text{NEQ}} \quad (40)$$

and

$$\bar{\mathbf{T}}^{\text{EQ}} = \frac{\partial \bar{\mathbf{S}}^{\text{EQ}}}{\partial \theta}, \quad \bar{\mathbf{T}}^{\text{NEQ}} = \frac{\partial \bar{\mathbf{S}}^{\text{NEQ}}}{\partial \theta}. \quad (41)$$

- The volumetric part.

$$\mathbf{T}_{\text{vol}} = \frac{\partial \mathbf{S}_{\text{vol}}}{\partial \theta}. \quad (42)$$

- The thermal part.

$$\mathbf{T}^{\theta} = \frac{\partial \mathbf{S}^{\theta}}{\partial \theta}. \quad (43)$$

4.1.2 Thermal material laws

The classic internal energy conservation law integrating over the entire volume in the current state reads

$$\int_{\Omega} \rho \dot{U} \mathrm{dv} = \int_{\partial \Omega} q \mathrm{ds} + \int_{\Omega} r \mathrm{dv}, \quad (44)$$

where ρ is the material density, $\dot{U}$ is the power of internal thermal energy U, $\partial \Omega$ is the surface of the continuum Ω at the current configuration, $q = -\mathbf{q} \cdot \mathbf{n}$ ($\mathbf{q}$ is the heat flux vector and $\mathbf{n}$ is the unit outward normal vector of the surface of Ω) is the heat flux into Ω per unit time, and r is the natural heat source inside Ω per unit time, respectively. By using Gauss's theorem and the Newton method, the weak form of Equation 44 is expressed as

$$\frac{1}{\Delta t}\int_{V} \delta\theta\rho\frac{\partial \Delta U}{\partial \theta}\theta dV + \frac{1}{\Delta t}\int_{V}\delta\theta\rho\frac{\partial \Delta U}{\partial \nabla\theta}\nabla\theta dV$$
$$+ \int_{V}(\delta\nabla\theta)\frac{\partial \mathbf{q}}{\partial \theta}\theta dV + \int_{V}(\delta\nabla\theta)\frac{\partial \mathbf{q}}{\partial \nabla\theta}\nabla\theta dV - \int_{S}\delta\theta\frac{\partial q}{\partial \theta}\theta dS$$
$$- \int_{V}\delta\theta\frac{\partial r}{\partial \theta}\theta dV = 0, \quad (45)$$

where $\delta\theta$ is the virtual temperature, $\delta\nabla\theta$ is the virtual temperature gradient, and $\nabla\theta$ is the temperature gradient. For the proposed constitutive framework,

- U is only the function of temperature,
- no natural heat source exists during the deformation,
- the heat flux is not affected by the temperature value,

are assumed. Therefore, once the spatial thermal conductivity

$$\boldsymbol{\kappa} \stackrel{\text{def}}{=} -\frac{\partial \mathbf{q}}{\partial \nabla\theta} \quad (46)$$

and specific heat capacity

$$c \stackrel{\text{def}}{=} \frac{\partial \Delta U}{\partial \theta} \quad (47)$$

are given, the internal energy conservation law (Equation 44) is solved. Note that for a thermally isotropic material, $\boldsymbol{\kappa}$ is an isotropic tensor, i.e., $\boldsymbol{\kappa} = k\mathbf{I}$, where k denotes the coefficient of the thermal conductivity defined according to the Fourier's law of heat conduction $\mathbf{q} = k\nabla\theta$. The thermal parameters of EPU are cited from other studies, as shown in Table 5.

4.2 Flow chart of the numerical algorithm

The algorithm framework is elucidated in this section for a more clear understanding of the finite element implementation. We should note that within a finite element algorithm, variables are updated iteratively. For each increment, the task of UMAT is to update the variable at the end of the current increment (denoted

Table 5

Thermal parameters.

Parameters	Value
Thermal expansion coefficient (α)	14×10^{-5} K^{-1} [12]
Thermal conductivity (k)	0.29 Wm^{-1} K^{-1} [69]
Specific heat capacity (c)	0.42×10^3 J g^{-1} K^{-1} [12]
Emissivity	0.95 [70]

as $\{\bullet\}_{n+1}$) based on the variable at the beginning of the same increment (denoted as $\{\bullet\}_n$). It is important to clarify that $\{\bullet\}_n$ are already updated at the end of the previous increment, and then passed into the current increment for information. These include, but are not limited to, the time increment Δt, temperature at the beginning of the increment $\{\theta\}_n$, the deformation gradient at the beginning of the increment $\{\mathbf{F}\}_n$, the deformation gradient at the end of the increment $\{\mathbf{F}\}_{n+1}$, and the user-defined variable at the beginning of the increment $\{\mathbf{C}_j^v\}_n$. It is important to note that time-dependent variables like $\mathbf{F}_e$ and $\mathbf{F}_v$ have inter-dependencies ($\bar{\mathbf{F}} = \mathbf{F}_e \mathbf{F}_v$). Therefore, in our algorithm, we only consider $\mathbf{C}_j^v$ as the user-defined variable that necessitates updating. In our framework, the updating process is mainly divided into four steps:

1) Firstly, the kinematic variables are determined according to Table 2. For instance, given the deformation gradient $\{\mathbf{F}\}_{n+1}$, its determinant is calculated to obtain $\{J\}_{n+1}$, and its tensor invariants are calculated to obtain $\{I_1\}_{n+1}$, $\{I_2\}_{n+1}$, and $\{I_3\}_{n+1}$. The isochoric variables, such as $\{\bar{\mathbf{F}}\}_{n+1}$ and $\{\bar{\mathbf{C}}\}_{n+1}$, could then be obtained. From the input of UMAT from the last increment, the value of $\{\mathbf{C}_j^v\}_n$ is a known quantity, and $\{\mathbf{C}_j^v\}_{n+1}$ is updated based on its evolution equation.

2) The next step involves the calculation of the Cauchy stress, as per the requirement of UMAT. Note that the stress calculation is based on the kinematic variables at the end of the increment, e.g., $\{\mathbf{F}\}_{n+1}$. According to our constitutive framework, we calculate the second Piola-Kirchhoff stress tensor, and then push-forward it to the spatial description to obtain the Cauchy stress tensor.

3) Subsequently, we calculate the referential elasticity tensor and the referential stress-temperature tensor, and then push-forward them to the spatial Jaumann tangent moduli and the spatial stress-temperature tensor, respectively, as required by UMAT.

4) Lastly, the volumetric heat generation per unit time at the end of the increment is calculated.

The flow chart is presented in Table 6 to facilitate a further understanding of the finite element implementation.

4.3 Validation of the finite element implementation

As a first step, simulations of homogeneous deformations are conducted for a validation purpose due to the simplicity of the deformation pattern and this choice facilitates a meaningful comparison with analytical results, such as those obtained from MATLAB. The specimen used in the validation process is a cuboid structure, with 25 mm in length, 2.5 mm in width, and 1.5 mm in thickness, as depicted in Figure 6. Note that this specimen is loaded along the X-direction, with the left-end surface restricted from displacement in the X-direction.

Table 6

Flow chart of the full algorithm for FEM implementation.

Input: At the beginning of the increment: Δt, $\{\theta\}_n$, $\{\mathbf{F}\}_n$, $\{\mathbf{F}\}_{n+1}$, $\{\mathbf{C}^v_j\}_n$

01: Kinematic variables determination.	▷ Table 2
02: Calculate $\bar{\mathbf{S}}^{\text{EQ}}$ and $\bar{\mathbf{S}}^{\text{NEQ}}$	▷ Table 3 & Table 3
03: $\mathbf{S}_{\text{iso}} = J^{-2/3}\mathbb{P} : (\bar{\mathbf{S}}^{\text{EQ}} + \bar{\mathbf{S}}^{\text{NEQ}})$	▷ Equation 6
04: Calculate p^{vol} and p^{θ}	▷ Table 3
05: $\mathbf{S}_{\text{vol}} = Jp^{\text{vol}}\mathbf{C}^{-1}$	▷ Equation 7
06: $\mathbf{S}^{\theta} = Jp^{\theta}\mathbf{C}^{-1}$	▷ Equation 8
07: Assemble the second Piola-Kirchhoff stress tensor $\mathbf{S} = \mathbf{S}_{\text{iso}} + \mathbf{S}_{\text{vol}} + \mathbf{S}^{\theta}$	▷ Equation 5
08: Calculate the Cauchy stress $\sigma = \frac{1}{J}\mathbf{FSF}^{\mathsf{T}}$	
09: Calculate $\bar{\mathbb{C}}^{\text{EQ}}$ and $\bar{\mathbb{C}}^{\text{NEQ}}$	▷ Equation 35 & Equation 36
10: $\mathbb{C}_{\text{iso}} = \mathbb{P} : (\bar{\mathbb{C}}^{\text{EQ}} + \bar{\mathbb{C}}^{\text{NEQ}}) : \mathbb{P}^{\mathsf{T}} + \frac{2}{3}\text{Tr}(J^{-2/3}\bar{\mathbf{S}})\tilde{\mathbb{P}} - \frac{2}{3}(\mathbf{C}^{-1} \otimes \mathbf{S}_{\text{iso}} + \mathbf{S}_{\text{iso}} \otimes \mathbf{C}^{-1})$	▷ Equation 4.1.1
11: $\mathbb{C}_{\text{vol}} = (Jp^{\text{vol}} + J^2\frac{dp^{\text{vol}}}{dJ})\mathbf{C}^{-1} \otimes \mathbf{C}^{-1} - 2Jp^{\text{vol}}\mathbf{C}^{-1} \odot \mathbf{C}^{-1}$	▷Equation 37
12: $\mathbb{C}^{\theta} = (Jp^{\theta} + J^2\frac{dp^{\theta}}{dJ})\mathbf{C}^{-1} \otimes \mathbf{C}^{-1} - 2Jp^{\theta}\mathbf{C}^{-1} \odot \mathbf{C}^{-1}$	▷ Equation 38
13: Assemble the referential elasticity tensor $\mathbb{C} = \mathbb{C}_{\text{iso}} + \mathbb{C}_{\text{vol}} + \mathbb{C}^{\theta}$	▷ Equation 31
14: Calculate the spatial Jaumann tangent moduli $\overset{\triangledown}{\mathbb{C}} = 2\sigma \otimes \mathbf{I} + \frac{1}{J}\left[(\mathbf{F} \otimes \mathbf{F}^{\mathsf{T}}) : \mathbb{C} : (\mathbf{F}^{\mathsf{T}} \otimes \mathbf{F})\right]$	▷ Equation 29
15: Calculate $\bar{\mathbf{T}}^{\text{EQ}}$ and $\bar{\mathbf{T}}^{\text{NEQ}}$	▷ Equation 41
16: $\mathbf{T}_{\text{iso}} = J^{-2/3}\mathbb{P} : (\bar{\mathbf{T}}^{\text{EQ}} + \bar{\mathbf{T}}^{\text{NEQ}})$	▷ Equation 40
17: $\mathbf{T}_{\text{vol}} = \frac{\partial \mathbf{S}_{\text{vol}}}{\partial \theta}$	▷ Equation 42
18: $\mathbf{T}^{\theta} = \frac{\partial \mathbf{S}^{\theta}}{\partial \theta}$	▷ Equation 43
19: Assemble the referential fourth-order elasticity tensor $\mathbf{T} = \mathbf{T}_{\text{iso}} + \mathbf{T}_{\text{vol}} + \mathbf{T}^{\theta}$	▷ Equation 39
20: Calculate the spatial stress-temperature tensor $\mathbf{t} = \frac{1}{J}\mathbf{FTF}^{\mathsf{T}}$	▷ Equation 30
21: Calculate R and its derivations to the strain and temperature increments.	▷ Equation 12

Output: At the end of the increment: $\{\sigma\}_{n+1}$, $\{\overset{\triangledown}{\mathbb{C}}\}_{n+1}$, $\{\mathbf{t}\}_{n+1}$, $\{\mathbf{C}^v_j\}_{n+1}$, $\{R\}_{n+1}$

Fig. 6

The dimension and boundary condition of the cuboid structure used to validate the accuracy of the FEM implementation.

The numerical simulations employ the thermal-mechanically coupled 8-node hybrid element (C3D8HT) to simulate the almost incompressible behaviour. It should be noted that for this type of hybrid element, an additional degree of freedom, namely $\hat{J}$, is introduced to displace the actual volume change J. Consequently, two additional derivatives

$$\hat{K} = J\frac{\partial^2 \Psi(\hat{J})}{\partial \hat{J}^2} \tag{48}$$

and

$$\frac{\partial \hat{K}}{\partial \hat{J}} = J\frac{\partial^3 \Psi(\hat{J})}{\partial \hat{J}^3} \tag{49}$$

are involved based on the total hybrid formulation within the FEM implementation. Furthermore, heat convection is considered at the external surface of the specimen. The simulated results, including nominal strain and nominal stress along the X-direction, are then compared with the analytical results.

Figure 7 (a) to Figure 7(d) suggest that the FEM implementation reaches the same values when compared with analytical results. Note that the comparison ignores the consideration of thermal

stress ($\mathbf{S}^{\theta}$), as it is not accounted for in the analytical solution as mentioned before. After the comparison process, the results incorporating thermal stress are shown in Figure 8, revealing only a minor difference for each temperature. This observation aligns with expectations, given the relatively low thermal expansion characteristic for the EPU material.

So far, the validation of the thermal-mechanically coupled FEM implementation has been fully evaluated, presenting good results in accuracy. Additionally, it should be noted that all of the simulations reach almost quadratic convergence (see **Appendix B**).

4.4 Investigation of self-heating effects

Self-heating, a temperature-increasing process caused by internal dissipation during deformation, is a physical characteristic of viscoelastic material. It should be emphasised, that the heat generation is solely derived from the chosen Helmholtz strain energy and is consequently a complex function of the strain, strain rate, absolute temperature, and stress value.
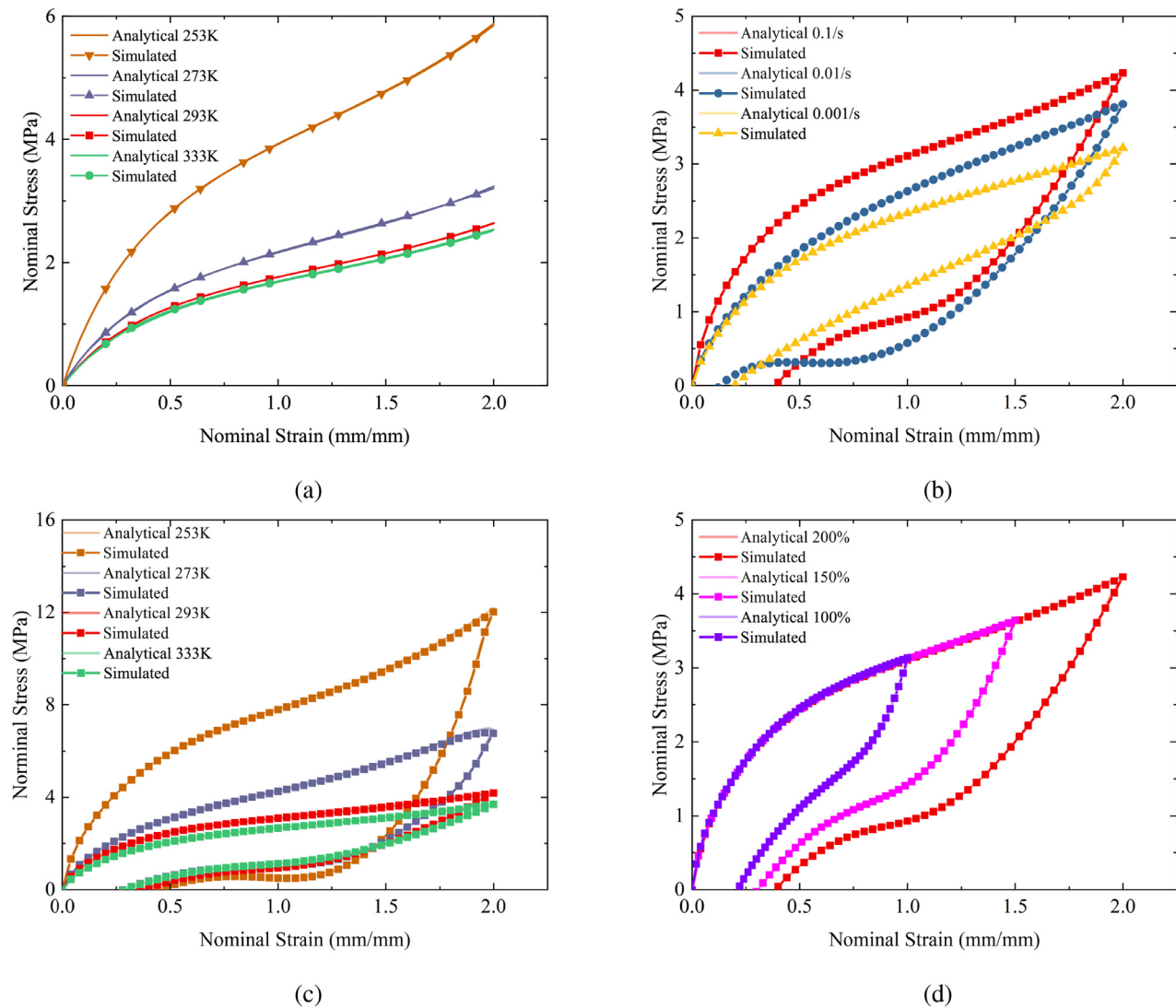
Fig. 7

FEM Implementation validation against analytical results from `MATLAB`. (a) The equilibrium paths under different temperatures. (b) The stress-strain curves at different strain rates. The temperature is 293K. (c) The stress-strain curves under different temperatures. The strain rate is 0.1/s. (d) The stress-strain curves under different maximum strain levels. The temperature is 293K and the strain rate is 0.1/s.

Figure 9 illustrates the temperature increase with regard to the strain relationship under 0.1/s and 0.001/s. Each rate case features two curves, namely the simulated temperature increase and the adiabatic temperature increase, respectively, depending on whether heat convection is considered. Some findings are listed below.

1. An adiabatic temperature increase of 4.99K is observed for the case of 0.1/s and 200% deformation, consistent with a previous study [12], where 4.27K was reported for polyurea (a soft material similar to EPU) at 0.08/s and 200% strain. Additionally, the adiabatic temperature increase is larger at 0.1/s compared to 0.001/s, reflecting increased internal dissipation.

2. Heat convection intensifies during large strain stages, attributed to the increasing convective surface area [12]. Furthermore, the diminishing strain rate results in a larger difference between simulated and adiabatic temperatures, influenced by the duration-dependent heat convection.

3. The inset in Figure 9(a) reveals endothermic behaviour for 0.001/s case, known as thermoelastic inversion [12,71–74]. This phenomenon suggests the competition between thermal expansion and entropy elasticity at small strains.

Figure 9(b) depicts temperature increase curves at various temperatures, with all simulations conducted at 0.1/s. The case for 253K exhibits the largest adiabatic temperature, which is attributed to the dominant internal dissipation at lower temperatures. Additionally, it is noteworthy that none of the curves presents endothermic behaviour, even at small strain stages (see the inset in Figure 9(b)). This absence is justifiable due to the non-negligible self-heating effect under 0.1/s even at a small strain stage.

5 Structural example

The objective of this section is to investigate the complex structural deformation to demonstrate the advantages of the FEM
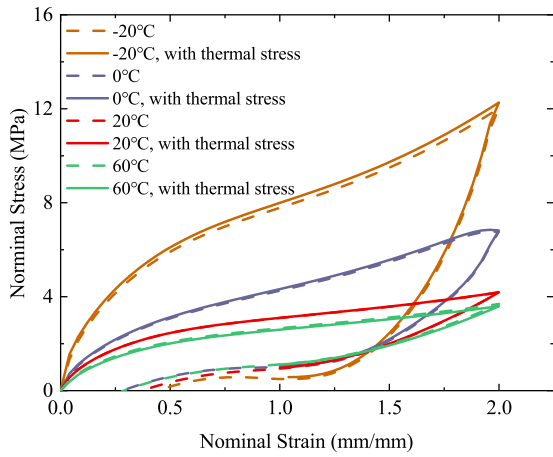
Fig. 8

The comparison between stress-strain curves after the incorporation of thermal stress.

Fig. 10

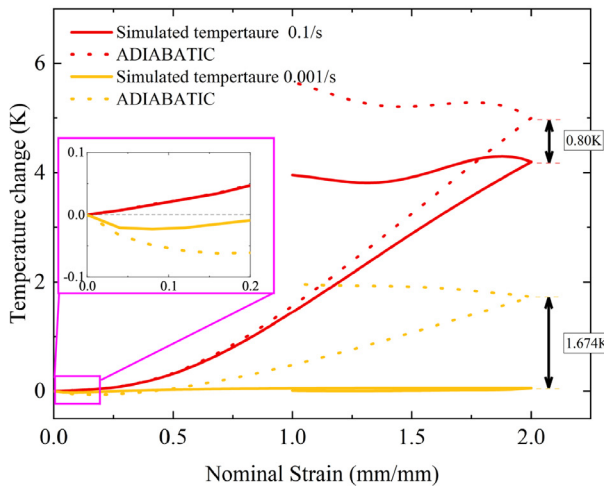The dimension and boundary conditions of the plate with a hole structure.

implementation. A plate with a hole, commonly employed to assess the robustness of any user-defined FEM codes [44,53,75–77], is selected here. Note that in contrast to the example discussed above, the deformation within the plate is non-uniform because of structural anisotropy.
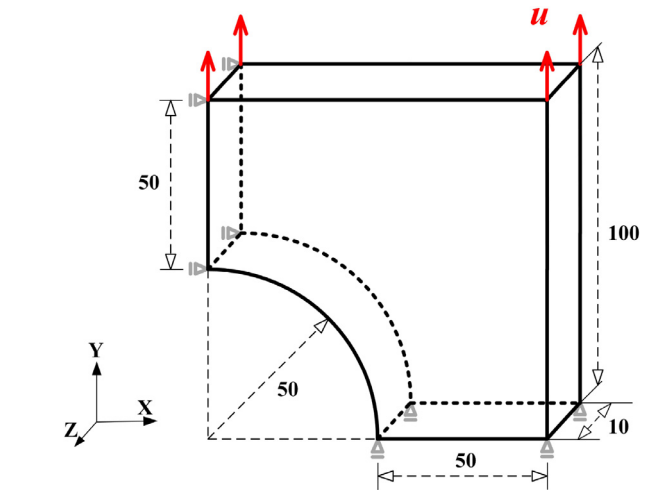
5.1 Numerical model

The dimension and boundary conditions of the plate structure are depicted in Figure 10.

Note that along the Y-direction, this specimen is subjected to a prescribed displacement u, with the bottom surface restricted from displacement in the Y-direction. Heat convection is considered at the specimen surface. The loading history is divided into two stages:

① the plate is loaded up u=100 mm at the top surface;

② then the plate is unloaded until the top surface recovers to its initial position.

With the utilisation of ABAQUS/Standard, the finite element simulation can be conducted with the user-developed constitutive model to this complex structure. Similar to the setup described in the above section, the C3D8HT element is selected for the following simulations. Furthermore, three mesh cases, i.e., Mesh1 ($n_{elem} = 120$), Mesh2 ($n_{elem} = 256$), and Mesh3 ($n_{elem} = 1932$), are considered to investigate the effect of spatial discretisation. The simulation schedule is detailed in Table 7.

5.2 Numerical results

5.2.1 Spatial discretisation

The effect of spatial discretisation is first investigated under 293K. The force-displacement relationships and the maximum

(a)
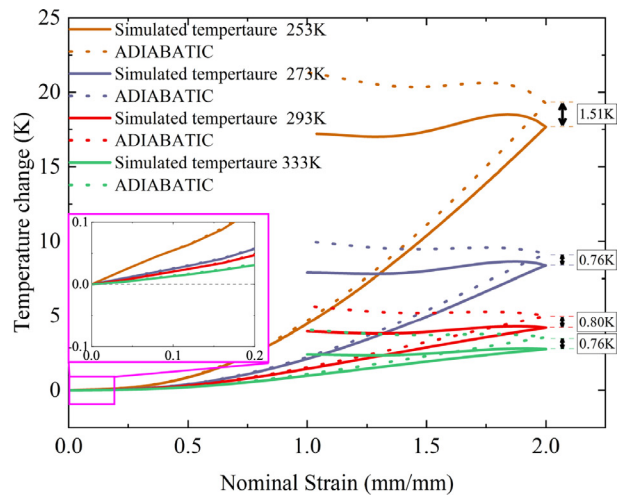
(b)

Fig. 9

Simulated and adiabatic temperature increases for (a) different strain rates and (b) different temperatures.

Table 7

The simulation schedule for the plate with a hole structure.

Deformation mode	Velocity [mm/s]	Holding time	Maximum prescribed displacement [mm]	Temperature			
				253K	273K	293K	333K
Uniaxial tension	5	–	100	●	●	●	●
Single-step stress relaxation	5	3 mins	100	●	–	–	–

(a) (b)
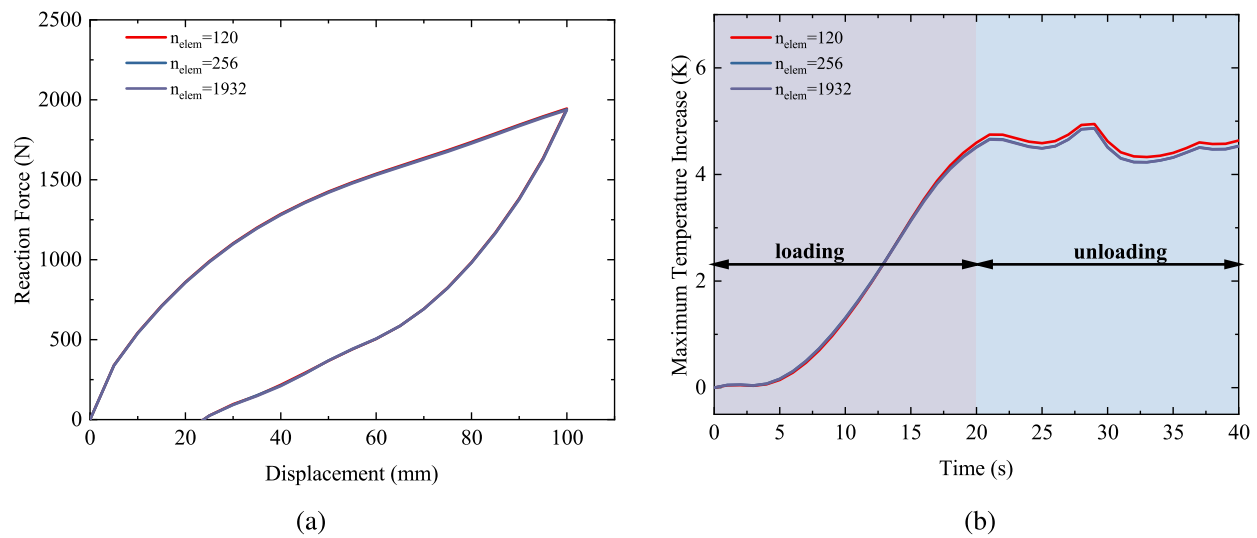
Fig. 11

(a) The force-displacement relationships for the plate with a hole structure under different spatial discretisations. (b) The maximum temperature increase for the plate with a hole structure under different spatial discretisations.

(a) (b)
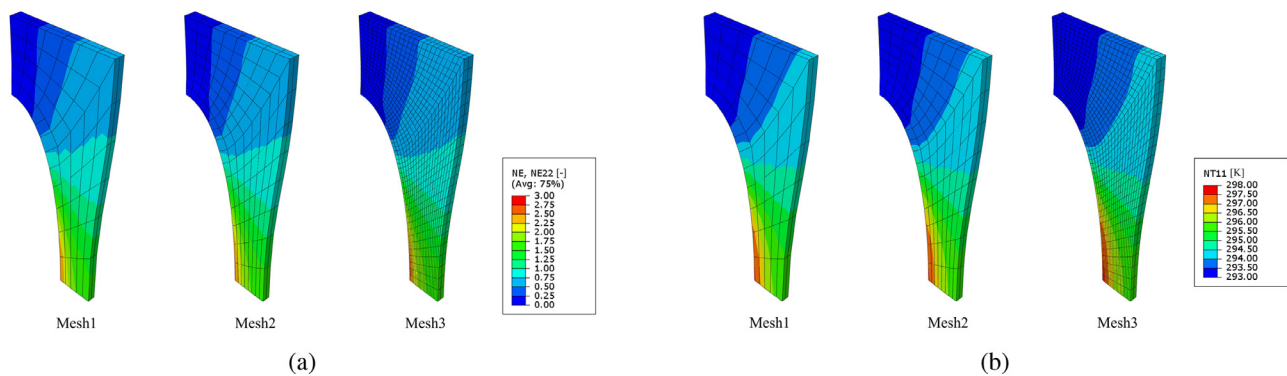
Fig. 12

Contours of Figure 12(a) the axial strain distribution and (b) the temperature distribution at u=100 mm for three different spatial discretisations: (Mesh1) n_{elem} = 120, (Mesh2) n_{elem} = 256, and (Mesh3) n_{elem} = 1932.

temperature increase for different spatial discretisations are shown in Figure 11(a) and Figure 11(b), respectively. Here, the reaction force represents the resultant reaction force in the Y-direction related to all the nodes on the top surface of the specimen. The results presented in these two figures show that the load-displacement responses almost completely coincide, with only a small difference in the maximum temperature rise shown in the unloading stage. This finding suggests that Mesh1 is coarse, while the other two mesh cases exhibit minimal differences in both the

force-displacement relationships and the maximum temperature values. Furthermore, contours of the axial strain distribution and the temperature distribution at u=100mm for three different spatial discretisations are shown in Figure 12(a) and Figure 12(b), respectively. It turns out that, for this particular specimen, the strain evolution, as well as the temperature distribution, is almost mesh-independent. Therefore, Mesh2 is chosen for the following analysis with the consideration of the smoothness of the contour and the computational cost (refer to Table 8).
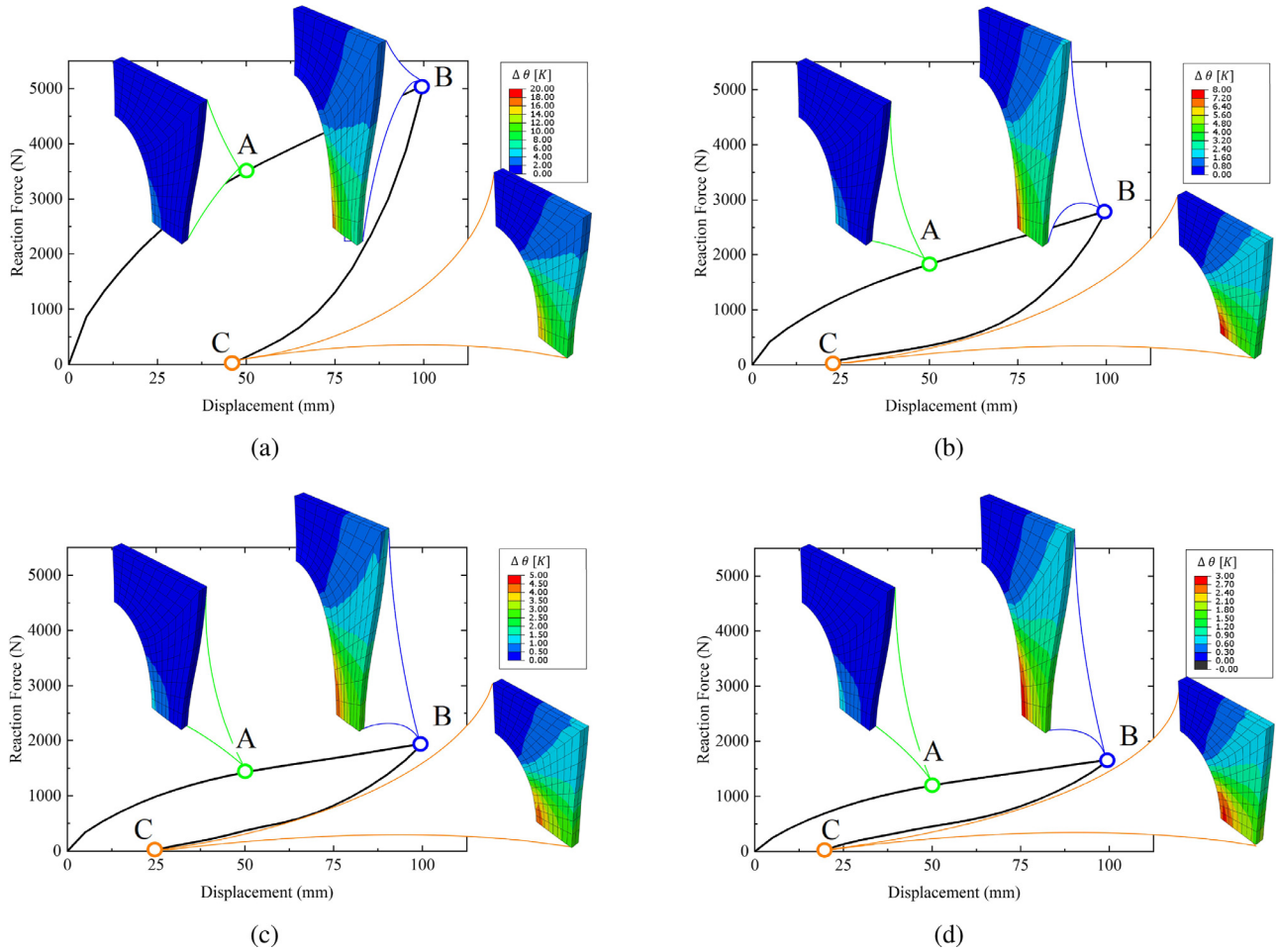
Fig. 13

Reaction force displacement relation and contours of temperature increase $\Delta\theta$ under (a) 253K, (b) 273K, (c) 293K, and (d) 333K, respectively.
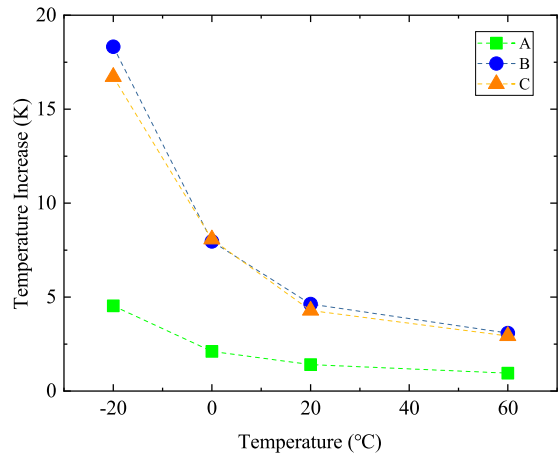
Table 8

The computational cost in terms of the CPU-time for uniaxial tension simulations under different spatial discretisations. Note that the simulations are based on the single-core mode of ABAQUS2023 on a CPU with the AMD Ryzen 7 5800H processor.

	Mesh1	Mesh2	Mesh3
Time [s]	122	242	754

Fig. 14

The maximum temperature increase values under different temperature cases for different stages, i.e., A, B, and C.

5.2.2 Load displacement response

The mechanical response of this structure is illustrated by the load-displacement curves shown in Figure 13(a), Figure 13(b), Figure 13(c), and Figure 13(d) for different temperatures, respectively.

It becomes apparent that the loading-unloading is associated with the dissipation of energy, manifesting by the characteristic hysteresis behaviour represented by the area enclosed by the loading and unloading curve. Three points denoted as *A* (u=50mm), *B* (u=100mm), and *C* (the free force state), are selected from the load-displacement curve to track the evolution

of the temperature increase distribution. The description of the temperature increase distribution for these three points is as follows.
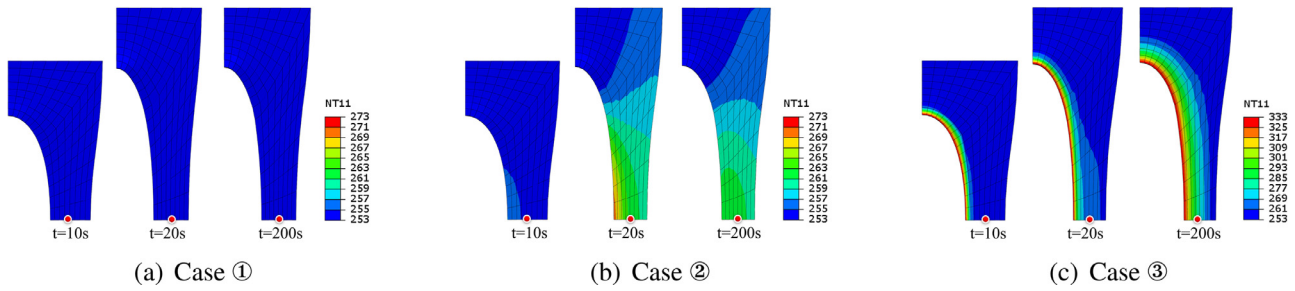
Fig. 15

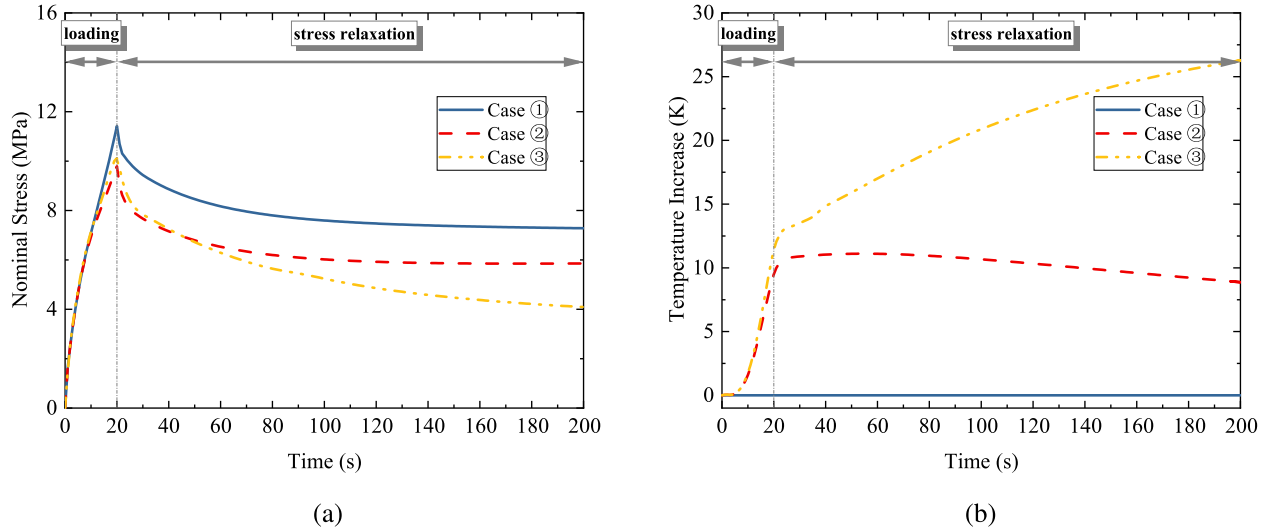Temperature distribution for different cases for selected time steps.

Fig. 16

(a) The nominal stress time relation for the single-step relaxation simulations. (b) The temperature increase time relation for the single-step relaxation simulations.

A. At point *A*, the temperature increase at each temperature is marginal, with the peak value situated around the bottom edge of the specimen, corresponding to the place with the highest strain (not plotted here). This aligns with the stress (or strain)-driven self-heating formulation.

B. Subsequently, at point *B*, the temperature increase reaches almost the maximum extent throughout the whole deformation process. The peak temperature increase position coincides with that mentioned in point *A*. For the 253K case, the maximum temperature rise can reach up to 18K. This observation is as expected because of the large hysteresis phenomenon occurring at low temperatures (refer to Figure 2(d)). The maximum temperature rise extent also correlates with the specimen's initial temperature (see the blue line of Figure 14). The lower the specimen initial temperature, the more pronounced the temperature rise at point *B*.

C. Finally, after the top surface returns to its force-free state, the residual temperature distribution can be seen at point *C*. The maximum temperature increase values at this point for 253K, 273K, 293K, and 333K are 16.71K, 8.07K, 4.29K, and 2.93K, respectively (similar to the situation at point *B*, see Figure 14).

5.2.3 Single-step stress relaxation

In this section, single-step stress relaxation simulations at 253K are considered, encompassing three cases:

①. simulation without considering the self-heating effect;

②. simulation incorporating the self-heating effect;

③. simulation considering the self-heating effect, with an additional temperature boundary (333K) applied at the edge of the hole. This implies that the specimen will experience heating up to 333K during the simulation.

Three time points are selected for each case, namely t=10s (the half of the loading), t=20s (the end of the loading), and t=200s (the end of the stress relaxation). The comparison among these cases and time steps provides clearer insights into the effects of self-heating and heat transfer. The temperature distributions at selected time points for these cases are plotted in Figure 15. In case ①, where the self-heating effect is neglected, no temperature change is observed inside the specimen during the whole simulation process. For case ②, temperature increases, especially near the edge of the hole, propagating throughout the specimen. The temperature rises during the loading stage because of the self-heating effect and then decreases during the holding stage mainly due to heat convection. After applying the

additional temperature boundary in case ③, the temperature rise becomes obvious, observable even at t=10s, and continues to spread towards other borders from t=20s to t=200s. This is the result of the classic heat transfer effect.

For quantitative tracking, one node of the specimen (marded in Figure 15) is used. Figure 16(a) and Figure 16(b) depict the stress and temperature time relations for all cases. In case ①, a typical stress relaxation curve is observed, where the stress decreases over time during the stress relaxation stage. In this case, the temperature of the specimen remains constant throughout the simulation. Then, with the consideration of the self-heating effect in case ②, the nominal stress follows a similar trend but with a lower value than in case ① due to the increased temperature. The corresponding temperature has a decreasing trend during the holding stage (t=20s to t=200s) due to reduced heat generation and sustained heat convection. Finally, in case ③, the nominal stress has a similar value to case ② during the loading stage but a slightly higher value of stress because of the larger thermal stress. Heat transfer has little influence on the structure at the loading stage (short duration). During the stress relaxation stage, the stress decreases more rapidly because of the quickly increased temperature caused by the heat transfer effect. It is reasonable to infer that, with infinite observation time, the entire specimen will be heated to 333K, and reach equilibrium.

6 Conclusion

In summary, this study introduces a thermo-mechanically coupled constitutive model for EPU, incorporating hyperelasticity, viscoelasticity, thermal expansion, and self-heating in a thermodynamically consistent manner. Based on experimental data obtained from our previous studies, model parameters are identified through the least squares method, with iterative updates for temperature parameters considering the self-heating effect. Subsequently, the validated model is implemented into the `UMAT` subroutine of `ABAQUS` to compute three-dimensional stress-strain states, facilitating the visualisation of structural responses under various mechanical loads and boundary conditions. The self-heating effect, incorporating mechanical work and viscoelastic dissipation, is then systematically analysed under different strain rates and temperatures, enhancing the comprehension of EPU's thermal-mechanical response to diverse conditions. Furthermore, a plate with a hole is simulated to shed light on the complex structural performance of EPU and present the engineering significance of FEM implementation of the proposed model. In conclusion, this research provides a valuable tool for engineers and researchers, fostering a deeper understanding and prediction of thermal-mechanical material behaviour in diverse scenarios. Future work will focus on applying the constitutive model to more complex structures (e.g., metamaterial) and more loading conditions (e.g., impact loading).

Declaration of competing interest

The authors declare that they have no known competing financial interests or personal relationships that could have appeared to influence the work reported in this paper.

Data availability

Data will be made available on request.

CRediT authorship contribution statement

Jie Yang: Writing – original draft, Visualization, Software, Investigation, Formal analysis. **Zisheng Liao:** Writing – review & editing, Writing – original draft, Methodology, Investigation, Conceptualization. **Deepak George:** Formal analysis, Software. **Mokarram Hossain:** Writing – review & editing, Writing – original draft, Supervision, Funding acquisition, Formal analysis, Conceptualization. **Xiaohu Yao:** Supervision, Funding acquisition.

Acknowledgements

Appendix A discussion about the incompressibility of the internal variable

In parameter identification, the evolution function of $\mathbf{C}^v$ is reduced into the one-dimensional case by using the Euler Backward Method (EBM) as

$$
\begin{aligned}
\{\lambda_1^v\}_{n+1} &= \{\lambda_1^v\}_n + \Delta t \left\{ \frac{1}{2\tau} \left[\frac{\lambda^2}{\lambda_1^v} - \lambda_1^v \right] \right\}_{n+1} \\
\{\lambda_2^v\}_{n+1} &= \{\lambda_2^v\}_n + \Delta t \left\{ \frac{1}{2\tau} \left[\frac{1}{\lambda\lambda_2^v} - \lambda_2^v \right] \right\}_{n+1} \\
\{\lambda_3^v\}_{n+1} &= \{\lambda_3^v\}_n + \Delta t \left\{ \frac{1}{2\tau} \left[\frac{1}{\lambda\lambda_3^v} - \lambda_3^v \right] \right\}_{n+1},
\end{aligned}
\tag{50}
$$

where

$$
\Delta t = \{t\}_{n+1} - \{t\}_n
\tag{51}
$$

and λ_1^v, λ_2^v, and λ_3^v are the eigenvalues of $[\mathbf{C}^v]^{1/2}$, respectively.

Furthermore, the differences between the stress-strain results by applying the strict incompressibility (SI) and almost incompressibility (AI) of internal variables are compared in this section. In other words, there are two approaches for determining the hydrostatic pressure p, leading to two sets of stress results.

- If the strict incompressibility is considered, the second and third equations of Equation 50 are not necessary to be solved since in this situation, we have

$$
\mathbf{C}^v = \begin{bmatrix} (\lambda^v)^2 & 0 & 0 \\ 0 & (\lambda^v)^{-1} & 0 \\ 0 & 0 & (\lambda^v)^{-1} \end{bmatrix}
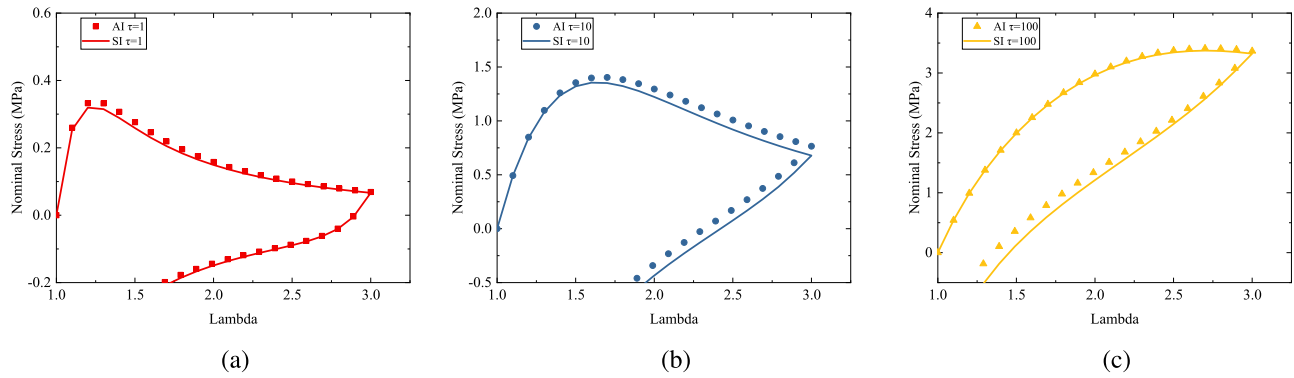\tag{52}
$$

(a)

(b)

(c)

Fig. 17

Comparison between $[P_{11}^{\mathrm{NEQ}}]^{\mathrm{SI}}$ and $[P_{11}^{\mathrm{NEQ}}]^{\mathrm{AI}}$ under different relaxation times.

Table 9

The Euclidean norm of the largest residual force for the cuboid and the plate with a hole structures at selected time points.

	Iteration	LARGEST RESIDUAL FORCE			
		5 [s]	10 [s]	15 [s]	20 [s]
Cuboid	1	4.674E-4	5.833E-6	4.198E-4	1.008E-4
	2	3.131E-10	1.382E-9	2.819E-9	3.538E-10
Plate with a hole	1	1.787E-02	7.511E-03	7.906E-03	9.628E-03
	2	2.782E-06	1.121E-06	4.923E-07	4.610E-06
	3	5.621E-11	2.719E-11	3.296E-11	3.001E-11

where $\lambda_1^v = \lambda^v$, $\lambda_2^v = \lambda_3^v = (\lambda^v)^{-1/2}$. The corresponding nominal stress is

$$[P_{11}^{\mathrm{NEQ}}]^{\mathrm{SI}} = 2c\left[\frac{\lambda}{[\lambda^v]^2} - \frac{[\lambda^v]}{\lambda^2}\right] \tag{53}$$

Note that for simplicity, the temperature influence is neglected here.

• If the almost incompressibility is considered,

$$\mathbf{C}^v = \begin{bmatrix} (\lambda_{11}^v)^2 & 0 & 0 \\ 0 & (\lambda_{22}^v)^2 & 0 \\ 0 & 0 & (\lambda_{33}^v)^2 \end{bmatrix} \tag{54}$$

The nominal stress is written as

$$[P_{11}^{\mathrm{NEQ}}]^{\mathrm{AI}} = 2c\left[\frac{\lambda}{(\lambda_{11}^v)^2} - \frac{1}{(\lambda_{22}^v)^2\lambda^2}\right] \tag{55}$$

The results are compared to see the differences between $[P_{11}^{\mathrm{NEQ}}]^{\mathrm{SI}}$ and $[P_{11}^{\mathrm{NEQ}}]^{\mathrm{AI}}$. Without loss of generality, the values of c are chosen as 1 for both cases, while τ is chosen as 1, 10, and 100. The comparisons, as plotted in Figure 17, show that there are indeed slight differences between the two cases.

Therefore, for consistency with the FEM implementation, during the one-dimensional reduction in Section 3, $\mathbf{C}^v$ is solved with almost incompressibility. We need to state here that both cases are correct, depending on the specific problem considered.

Appendix B the convergence situation

The convergence situation is checked for two structures, i.e., the cuboid and the plate with a hole, which is used in the above sections. The loading velocity is controlled to promise the maximum strain and the strain rate inside each structure is around 200% and 0.1/s, respectively. The updates of the Euclidean norm of the largest residual force with the Newton iteration are listed in Table 9. We should note that the convergence situations for both structures show approximate quadratic convergence, presenting the consistency of the tangent derivation to stress tensors.

References

[1] D. Chattopadhyay, K. Raju, Structural engineering of polyurethane coatings for high performance applications, Progress in Polymer Science 32 (3) (2007) 352–418, doi:10.1016/j.progpolymsci.2006.05.003.

[2] H. Somarathna, S. Raman, D. Mohotti, A. Mutalib, K. Badri, Rate dependent tensile behavior of polyurethane under varying strain rates, Construction and Building Materials 254 (2020) 119203, doi:10.1016/j.conbuildmat.2020.119203.

[3] M. Hossain, R. Navaratne, D. Perić, 3D printed elastomeric polyurethane: Viscoelastic experimental characterizations and constitutive modelling with nonlinear viscosity functions, International Journal of Non-Linear Mechanics 126 (2020) 103546, doi:10.1016/j.ijnonlinmec.2020.103546.

[4] J. Yang, Z. Liao, M. Hossain, G. Huang, K. Wang, X. Yao, Thermo-mechanical experimental investigations of 3D-printed elastomeric polyurethane from low to intermediate strain rates, Mechanics Research Communications 134 (2023) 104212, doi:10.1016/j.mechrescom.2023.104212.

[5] J. Yang, Z. Liao, M. Hossain, G. Huang, X. Zhou, F. Liu, A.S. Alzaidi, X. Yao, Thermo-mechanical properties of digitally-printed elastomeric polyurethane: Experimental characterisation and constitutive modelling using a nonlinear temperature-strain coupled scaling strategy, International Journal of Solids and Structures 267 (2023) 112163, doi:10.1016/j.ijsolstr.2023.112163.

[6] Z.S. Petrović, J. Ferguson, Polyurethane elastomers, Progress in Polymer Science 16 (5) (1991) 695–836, doi:10.1016/0079-6700(91)90011-9.

[7] H. Qi, Constitutive model for stretch-induced softening of the stress-stretch behavior of elastomeric materials, Journal of the Mechanics and Physics of Solids 52 (10) (2004) 2187–2205, doi:10.1016/j.jmps.2004.04.008.

[8] H. Qi, M. Boyce, Stress–strain behavior of thermoplastic polyurethanes, Mechanics of Materials 37 (8) (2005) 817–839, doi:10.1016/j.mechmat.2004.08.001.

[9] A.V. Amirkhizi, J. Isaacs, J. McGee, S. Nemat-Nasser, An experimentally-based viscoelastic constitutive model for polyurea, including pressure and temperature effects, Philosophical Magazine 86 (36) (2006) 5847–5866, doi:10.1080/14786430600833198.

[10] S. Raman, T. Ngo, J. Lu, P. Mendis, Experimental investigation on the tensile behavior of polyurea at high strain rates, Materials & Design 50 (2013) 124–129, doi:10.1016/j.matdes.2013.02.063.

[11] L. Zhang, X. Yao, S. Zang, Q. Han, Temperature and strain rate dependent tensile behavior of a transparent polyurethane interlayer, Materials & Design (1980-2015) 65 (2015) 1181–1188, doi:10.1016/j.matdes.2014.08.054.

[12] P. Mott, C. Giller, D. Fragiadakis, D. Rosenberg, C. Roland, Deformation of polyurea: Where does the energy go? Polymer 105 (2016) 227–233, doi:10.1016/j.polymer.2016.10.029.

[13] M. Nikoukalam, P. Sideris, Experimental characterization and constitutive modeling of polyurethanes for structural applications, accounting for damage, hysteresis, loading rate and long term effects, Engineering Structures 198 (2019) 109462, doi:10.1016/j.engstruct.2019.109462.

[14] Y. Miao, H. Zhang, H. He, Q. Deng, Mechanical behaviors and equivalent configuration of a polyurea under wide strain rate range, Composite Structures 222 (2019) 110923, doi:10.1016/j.compstruct.2019.110923.

[15] Z. Liao, X. Yao, L. Zhang, M. Hossain, J. Wang, S. Zang, Temperature and strain rate dependent large tensile deformation and tensile failure behavior of transparent polyurethane at intermediate strain rates, International Journal of Impact Engineering 129 (2019) 152–167, doi:10.1016/j.ijimpeng.2019.03.005.

[16] H. Somarathna, S. Raman, D. Mohotti, A. Mutalib, K. Badri, Hyper-viscoelastic constitutive models for predicting the material behavior of polyurethane under varying strain rates and uniaxial tensile loading, Construction and Building Materials 236 (2020) 117417, doi:10.1016/j.conbuildmat.2019.117417.

[17] B.E. Abali, M.Y. Yardımcı, M. Zecchini, G. Daissè, F.H. Marchesini, G. De Schutter, R. Wan-Wendner, Experimental investigation for modeling the hardening of thermosetting polymers during curing, Polymer Testing 102 (2021) 107310, doi:10.1016/j.polymertesting.2021.107310.

[18] C. Gong, Y. Chen, T. Li, Z. Liu, Z. Zhuang, B. Guo, H. Wang, L. Dai, Free volume based nonlinear viscoelastic model for polyurea over a wide range of strain rates and temperatures, Mechanics of Materials 152 (2021) 103650, doi:10.1016/j.mechmat.2020.103650.

[19] A. Esmaeili, D. George, I. Masters, M. Hossain, Biaxial experimental characterizations of soft polymers: A review, Polymer Testing 128 (2023) 108246, doi:10.1016/j.polymertesting.2023.108246.

[20] M. Mooney, A Theory of Large Elastic Deformation, Journal of Applied Physics 11 (9) (1940) 582–592, doi:10.1063/1.1712836.

[21] Ogden, Large deformation isotropic elasticity: On the correlation of theory and experiment for compressible rubberlike solids, Proc. R. Soc. Lond. A 328 (1575) (1972) 567–583, doi:10.1098/rspa.1972.0096.

[22] E.M. Arruda, M.C. Boyce, A three-dimensional constitutive model for the large stretch behavior of rubber elastic materials, Journal of the Mechanics and Physics of Solids 41 (2) (1993) 389–412, doi:10.1016/0022-5096(93)90013-6.

[23] C. Gamonpilas, R. McCuiston, A non-linear viscoelastic material constitutive model for polyurea, Polymer 53 (17) (2012) 3655–3658, doi:10.1016/j.polymer.2012.06.030.

[24] D. Mohotti, M. Ali, T. Ngo, J. Lu, P. Mendis, Strain rate dependent constitutive model for predicting the material behaviour of polyurea under high strain rate tensile loading, Materials & Design 53 (2014) 830–837, doi:10.1016/j.matdes.2013.07.020.

[25] G. Chevellard, K. Ravi-Chandar, K.M. Liechti, Modeling the Nonlinear Viscoelastic Behavior of Polyurea Using a Distortionmodified Free Volume Approach, in: T. Proulx (Ed.), Mechanics of Time-Dependent Materials and Processes in Conventional and Multifunctional Materials, Volume 3, Springer New York, New York, NY, 2011, doi:10.1007/978-1-4614-0213-8_34. 239–239

[26] M. Ju, H. Jmal, R. Dupuis, E. Aubry, Visco-hyperelastic constitutive model for modeling the quasi-static behavior of polyurethane foam in large deformation, Polym Eng Sci 55 (8) (2015) 1795–1804, doi:10.1002/pen.24018.

[27] R.J. Clifton, X. Wang, T. Jiao, A physically-based, quasilinear viscoelasticity model for the dynamic response of polyurea, Journal of the Mechanics and Physics of Solids 93 (2016) 8–15, doi:10.1016/j.jmps.2016.04.027.

[28] G.A. Holzapfel, Nonlinear Solid Mechanics: A Continuum Approach for Engineering, Wiley, Chichester ; New York, 2000.

[29] T. Jiao, R.J. Clifton, S.E. Grunschel, Pressure-sensitivity and constitutive modeling of an elastomer at high strain rates, AIP Conference Proceedings 1195 (1) (2009) 1229–1232, doi:10.1063/1.3295026.

[30] J. Shim, D. Mohr, Rate dependent finite strain constitutive model of polyurea, International Journal of Plasticity 27 (6) (2011) 868–886, doi:10.1016/j.ijplas.2010.10.001.

[31] H. Cho, R.G. Rinaldi, M.C. Boyce, Constitutive modeling of the rate-dependent resilient and dissipative large deformation behavior of a segmented copolymer polyurea, Soft Matter 9 (27) (2013) 6319, doi:10.1039/c3sm27125k.

[32] Y. Yuan, S. Wang, P. Tan, H. Zhu, Mechanical performance and shear constitutive model study of a new high-capacity polyurethane elastomeric bearing, Construction and Building Materials 232 (2020) 117227, doi:10.1016/j.conbuildmat.2019.117227.

[33] M. Hossain, Z. Liao, An additively manufactured silicone polymer: Thermo-viscoelastic experimental study and computational modelling, Additive Manufacturing 35 (2020) 101395, doi:10.1016/j.addma.2020.101395.

[34] T.M.E. Sayed, CONSTITUTIVE MODELS FOR POLYMERS AND SOFT BIOLOGICAL TISSUES143.

[35] S. Reese, A micromechanically motivated material model for the thermo-viscoelastic material behaviour of rubber-like polymers, International Journal of Plasticity 19 (7) (2003) 909–940, doi:10.1016/s0749-6419(02)00086-4.

[36] V. Srivastava, S.A. Chester, N.M. Ames, L. Anand, A thermo-mechanically-coupled large-deformation theory for amorphous polymers in a temperature range which spans their glass transition, International Journal of Plasticity 26 (8) (2010) 1138–1182, doi:10.1016/j.ijplas.2010.01.004.

[37] A.K. Sharma, A. Khurana, M.M. Joglekar, Finite Element Model for Investigating the Thermo-Electro-Mechanical Response of Inhomogeneously Deforming Dielectric Elastomer Actuators, TECM (2015), doi:10.13052/ejcm2642-2085.30464.

[38] J. Plagge, M. Klüppel, A physically based model of stress softening and hysteresis of filled rubber including rate- and temperature dependency, International Journal of Plasticity 89 (2017) 173–196, doi:10.1016/j.ijplas.2016.11.010.

[39] C. Yu, G. Kang, K. Chen, A hygro-thermo-mechanical coupled cyclic constitutive model for polymers with considering glass transition, International Journal of Plasticity 89 (2017) 29–65, doi:10.1016/j.ijplas.2016.11.001.

[40] L. Dai, C. Tian, R. Xiao, Modeling the thermo-mechanical behavior and constrained recovery performance of cold-programmed amorphous shape-memory polymers, International Journal of Plasticity 127 (2020) 102654, doi:10.1016/j.ijplas.2019.102654.

[41] J. Plagge, A. Ricker, N. Kröger, P. Wriggers, M. Klüppel, Efficient modeling of filled rubber assuming stress-induced microscopic restructurization, International Journal of Engineering Science 151 (2020) 103291, doi:10.1016/j.ijengsci.2020.103291.

[42] A. Bahrololoumi, V. Morovati, E.A. Poshtan, R. Dargazany, A multi-physics constitutive model to predict hydrolytic aging in quasi-static behaviour of thin cross-linked polymers, International Journal of Plasticity 130 (2020) 102676, doi:10.1016/j.ijplas.2020.102676.

[43] R. Xiao, T.-T. Mai, K. Urayama, J.P. Gong, S. Qu, Micromechanical modeling of the multi-axial deformation behavior in double network hydrogels, International Journal of Plasticity 137 (2021) 102901, doi:10.1016/j.ijplas.2020.102901.

[44] S. Felder, H. Holthusen, S. Hesseler, F. Pohlkemper, T. Gries, J.-W. Simon, S. Reese, Incorporating crystallinity distributions into a thermo-mechanically coupled constitutive model for semi-crystalline polymers, International Journal of Plasticity 135 (2020) 102751, doi:10.1016/j.ijplas.2020.102751.

[45] H. Yang, G. Ganzosch, I. Giorgio, B.E. Abali, Material characterization and computations of a polymeric metamaterial with a pantographic substructure, Z. Angew. Math. Phys. 69 (4) (2018) 105, doi:10.1007/s00033-018-1000-3.

[46] C. Miehe, Numerical computation of algorithmic (consistent) tangent moduli in large-strain computational inelasticity, Computer Methods in Applied Mechanics and Engineering 134 (3-4) (1996) 223–240, doi:10.1016/0045-7825(96)01019-5.

[47] R. Raghunath, D. Juhre, M. Klüppel, A physically motivated model for filled elastomers including strain rate and amplitude dependency in finite viscoelasticity, International Journal of Plasticity 78 (2016) 223–241, doi:10.1016/j.ijplas.2015.11.005.

[48] M. Freund, H. Lorenz, D. Juhre, J. Ihlemann, M. Klüppel, Finite element implementation of a microstructure-based model for filled elastomers, International Journal of Plasticity 27 (6) (2011) 902–919, doi:10.1016/j.ijplas.2010.10.003.

[49] W. Sun, E.L. Chaikof, M.E. Levenston, Numerical Approximation of Tangent Moduli for Finite Element Implementations of Nonlinear Hyperelastic Material Models, J. Biomech. Eng. 130 (6) (2008) 061003, doi:10.1115/1.2979872.

[50] F. Meier, C. Schwarz, E. Werner, Numerical calculation of the tangent stiffness matrix in materials modeling, Proc Appl Math and Mech 14 (1) (2014) 425–426, doi:10.1002/pamm.201410200.

[51] I. Collins, M. Contino, C. Marano, I. Masters, M. Hossain, On the influence of time-dependent behaviour of elastomeric wave energy harvesting membranes using experimental and numerical modelling techniques, European Journal of Mechanics - A/Solids 98 (2023) 104895, doi:10.1016/j.euromechsol.2022.104895.

[52] C. Ovalle Rodas, F. Zaïri, M. Naït-Abdelaziz, A finite strain thermo-viscoelastic constitutive model to describe the self-heating in elastomeric materials during low-cycle fatigue, Journal of the Mechanics and Physics of Solids 64 (2014) 396–410, doi:10.1016/j.jmps.2013.10.010.

[53] J. Johnsen, A.H. Clausen, F. Grytten, A. Benallal, O.S. Hopperstad, A thermo-elasto-viscoplastic constitutive model for polymers, Journal of the Mechanics and Physics of Solids 124 (2019) 681–701, doi:10.1016/j.jmps.2018.11.018.

[54] B.D. Coleman, M.E. Gurtin, Thermodynamics with Internal State Variables 47(2) 597–613. https://pubs.aip.org/jcp/article/47/2/597/84815/Thermodynamics-with-Internal-State-Variables. 10.1063/1.1711937

[55] M.M. Carroll, A Strain Energy Function for Vulcanized Rubbers, J Elast 103 (2) (2011) 173–187, doi:10.1007/s10659-010-9279-0.

[56] M. Destrade, G. Saccomandi, I. Sgura, Methodical fitting for mathematical models of rubber-like materials, Proc. R. Soc. A. 473 (2198) (2017) 20160811, doi:10.1098/rspa.2016.0811.

[57] A. Anssari-Benam, A. Bucchi, A generalised neo-Hookean strain energy function for application to the finite deformation of elastomers, International Journal

of Non-Linear Mechanics 128 (2021) 103626, doi:10.1016/j.ijnonlinmec.2020.103626.

[58] A. Anssari-Benam, C.O. Horgan, New constitutive models for the finite deformation of isotropic compressible elastomers, Mechanics of Materials 172 (2022) 104403, doi:10.1016/j.mechmat.2022.104403.

[59] K.C. Valanis, R.F. Landel, The Strain-Energy Function of a Hyperelastic Material in Terms of the Extension Ratios, Journal of Applied Physics 38 (7) (1967) 2997–3002, doi:10.1063/1.1710039.

[60] T. Sussman, K.-J. Bathe, A finite element formulation for nonlinear incompressible elastic and inelastic analysis, Computers & Structures 26 (1-2) (1987) 357–409, doi:10.1016/0045-7949(87)90265-3.

[61] J. Simo, R. Taylor, Penalty function formulations for incompressible nonlinear elastostatics, Computer Methods in Applied Mechanics and Engineering 35 (1) (1982) 107–118, doi:10.1016/0045-7825(82)90035-4.

[62] R. Ogden, Volume changes associated with the deformation of rubber-like solids, Journal of the Mechanics and Physics of Solids 24 (6) (1976) 323–338, doi:10.1016/0022-5096(76)90007-7.

[63] R.W. Ogden, Large deformation isotropic elasticity – on the correlation of theory and experiment for incompressible rubberlike solids, Proc. R. Soc. Lond. A 326 (1567) (1972) 565–584, doi:10.1098/rspa.1972.0026.

[64] K. Li, G.A. Holzapfel, Multiscale modeling of fiber recruitment and damage with a discrete fiber dispersion method, Journal of the Mechanics and Physics of Solids 126 (2019) 226–244, doi:10.1016/j.jmps.2019.01.022.

[65] K. Li, R.W. Ogden, G.A. Holzapfel, Modeling fibrous biological tissues with a general invariant that excludes compressed fibers, Journal of the Mechanics and Physics of Solids 110 (2018) 38–53, doi:10.1016/j.jmps.2017.09.005.

[66] C.O. Horgan, G. Saccomandi, Constitutive Models for Compressible Nonlinearly Elastic Materials with Limiting Chain Extensibility, J Elasticity 77 (2) (2004) 123–138, doi:10.1007/s10659-005-4408-x.

[67] O. Gültekin, H. Dal, G.A. Holzapfel, On the quasi-incompressible finite element analysis of anisotropic hyperelastic materials, Comput Mech 63 (3) (2019) 443–453, doi:10.1007/s00466-018-1602-9.

[68] Y. Navidtehrani, C. Betegón, E. Martínez-Pañeda, A simple and robust Abaqus implementation of the phase field fracture method, Applications in Engineering Science 6 (2021) 100050, doi:10.1016/j.apples.2021.100050.

[69] CJM. Lasance, The thermal conductivity of rubbers/elastomers, 2001, (https://www.electronics-cooling.com/2001/11/the-thermal-conductivity-of-rubbers-elastomers/).

[70] H. Haissoune, J.-M. Chenal, L. Chazeau, G. Sebald, I. Morfin, L. Lebrun, F. Dalmas, G. Coativy, Elastocaloric effect: Impact of heat transfer on strain-induced crystallization kinetics of natural rubber, Polymer 263 (2022) 125506, doi:10.1016/j.polymer.2022.125506.

[71] R.L. Anthony, R.H. Caston, E. Guth, Equations of state for natural and synthetic rubber-like materials. I. Unaccelerated natural soft rubber, J. Phys. Chem. 46 (8) (1942) 826–840, doi:10.1021/j150422a005.

[72] L.R.G. Treloar, The Physics of Rubber Elasticity, third edition, Oxford University Press, Manchester, 1975.

[73] P.J. Flory, Principles of Polymer Chemistry, The George Fisher Baker Non-Resident Lectureship in Chemistry at Cornell University, Cornell university press, Ithaca (N.Y.) London, 1992.

[74] G. Holzapfel, J. Simo, Entropy elasticity of isotropic rubber-like solids at finite strains, Computer Methods in Applied Mechanics and Engineering 132 (1-2) (1996) 17–44, doi:10.1016/0045-7825(96)01001-8.

[75] T. Waffenschmidt, C. Polindara, A. Menzel, S. Blanco, A gradient-enhanced large-deformation continuum damage model for fibre-reinforced materials, Computer Methods in Applied Mechanics and Engineering 268 (2014) 801–842, doi:10.1016/j.cma.2013.10.013.

[76] N.K. Jha, U. Nackenhorst, V.S. Pawar, R. Nadella, P. Guruprasad, On the constitutive modelling of fatigue damage in rubber-like materials, International Journal of Solids and Structures 159 (2019) 77–89, doi:10.1016/j.ijsolstr.2018.09.022.

[77] L. Zhan, S. Wang, S. Qu, P. Steinmann, R. Xiao, A new micro–macro transition for hyperelastic materials, Journal of the Mechanics and Physics of Solids 171 (2023) 105156, doi:10.1016/j.jmps.2022.105156.